약학박사학위논문

그래핀과 DNA 기반 생체재료의 활용을 통한 진단과 항암 치료 연구

Graphene and DNA based biomaterials for diagnosis and anticancer therapy

2020 년 2월

서울대학교 융합과학기술대학원
분자의학 및 바이오제약학과
분자의학 및 바이오제약학 전공

이 재 우

그래핀과 DNA 기반 생체재료의 활용을 통한 진단과 항암 치료 연구

Graphene and DNA based biomaterials for diagnosis and anticancer therapy

지도교수 변영로

이 논문을 약학박사학위논문으로 제출함
2020년 2월

서울대학교 융합과학기술대학원
분자의학 및 바이오제약학과
분자의학 및 바이오제약학 전공
이재우

이재우의 약학박사학위논문을 인준함
2020년 2월

위 원 장	신 영 기	(인)
부위원장	변 영 로	(인)
위 원	오 유 경	(인)
위 원	구 효 정	(인)
위 원	임 수 정	(인)

Abstract

Graphene and DNA based biomaterials for diagnosis and anticancer therapy

Jaiwoo Lee
Department of Molecular Medicine and
Biopharmaceutical Sciences,
Graduate School of Convergence Science,
Seoul National University

Here, we report a double-stranded, dual-anchored, fluorescent aptamer on reduced graphene oxide (rGO) for the sensitive, selective, and speedy detection of a target protein in biological samples. This nano detector is composed of a target protein-specific fluorescent aptamer with BHQ1 as one anchoring moiety that forms double-stranded sequences with a complementary oligonucleotide sequence with BHQ1 as the other anchoring moiety, anchored to rGO nanosheets. The double-stranded and dualanchored aptamer on rGO nanosheets (DAGO) exhibited 7.3-fold higher fluorescence intensities compared to a single-stranded, single-anchored fluorescent aptamer on rGO. As a model target protein, interferon-g was used. DAGO detected the target protein, with linearity over a five-orders-of-magnitude concentration range (0.1 ng/mle10 mg/ml) in buffer and human serum. DAGO was highly specific for the target protein, exhibiting little changes in fluorescence intensity in response to the non-target proteins, interleukin-2 and tumor necrosis factor-a. Moreover, DAGO allowed rapid quantification

of the target protein in human immunodeficiency virus-positive patient serum samples. DAGO-based detection was complete in less than 10 min. Our results indicate that the DAGO provides new opportunities for the rapid and specific detection of target proteins in biological samples and could be widely applied to quantitate various target proteins by replacing the aptamer sequences.

Second, we also report the non-covalent functionalization of reduced graphene oxide (rGO) nanosheets using chimeric peptides engineered to have a biologically functional sequence, a spacer sequence, and an rGO-binding sequence. As a model peptide with biological activity, the cell-penetrating peptide buforin IIb (Bu) was used. A stretch of seven consecutive phenylalanine residues (7F) was used as the rGO-binding sequence. The various effects of tetraglycine (4G) and tetra-aspartate (4D) as spacers between the biologically active Bu and the rGO-binding 7F sequences were compared. All the chimeric peptides had a-helical structures at the carboxyl-terminal sequence, showing a structural similarity to the a-helical structure of Bu alone. Free chimeric peptides composed of 7F-Bu, 7F4G-Bu, or 7F4D-Bu in solution exhibited cell-penetrating abilities similar to that of Bu alone. However, following attachment onto rGO nanosheets, the compositions of the chimeric peptides affected the biological activity of Bu. Following modification, the 7F4D-Bu chimeric peptide yielded a higher cellular uptake of the rGO nanosheets than the other chimeric peptides. The levels of cellular uptake of the rGO nanosheets modified with the chimeric peptides were further evaluated by measuring the photothermal effect after near-infrared laser irradiation. The cells treated with 7F4D-Bu-modified rGO showed the greatest increase in temperature upon irradiation, with the temperature reaching 58.3 °C. The 7F4D-Bu-modified rGO also exhibited the highest photothermal cell-killing activity upon near-infrared laser irradiation. Our results demonstrate the utility of chimeric peptide engineering for simple and facile one-step non-covalent modification of

rGO. The chimeric peptide composed of 7F4D can be further used to tether various functional peptides onto rGO nanosheets.

Lastly Immune checkpoint inhibitors have been widely studied in immunotherapy. Although antibodies have been more widely used to block immune checkpoints, DNA aptamers have unique advantages for this purpose. Here, we designed a DNA polyaptamer hydrogel that can be precisely cut by Cas9/sgRNA for programmed release of an immune checkpoint-blocking DNA aptamer. As a representative immune checkpoint inhibitor, we used a PD-1DNA aptamer. Rolling-circle amplification was used to generate a hydrogel comprising DNA with PD-1 aptamer and an sgRNA-targeting sequence. When mixed with Cas9/sgRNA, the PD-1 DNA aptamer hydrogel (PAH) lost its gel property and liberated the PD-1 aptamer sequence. The precise Cas9/sgRNA-mediated release of the PD-1 DNA aptamer, which was confirmed by gel electrophoresis, was found to effectively activate the cytokine-secretion function of splenocytes. In vivo, molecular imaging revealed that PD-1 DNA polyaptamer hydrogel coinjected with Cas9/sgRNA (Cas9/PAH) remained at the injection site longer than free aptamer and yielded significantly higher antitumor effects and survival than hydrogel or free aptamer. Moreover, increased immune cell filtration was observed at tumor tissues treated with Cas9/PAH. These results suggest that our Cas9/sgRNAedited immune checkpoint-blocking aptamer hydrogel has strong potential for anticancer immunotherapy.

Keywords: Graphene oxide, Diagnosis, Chimeric peptide, Photothermal therapy, Cas9 editing, PD1 DNA polyaptamer hydrogel, Immune checkpoint blockade, Immunotherapy

Student Number : 2011-23064

Contents

List of Tables

List of Figures

Chapter I

Overview

1. Introduction

Graphene-based nanosheets have received wide attention due to their potential applications in biomedical fields, [1, 2] including drug delivery, [3] tissue engineering, [4] and biosensors. [5] They have also been modified with polymers, [6] lipids, [7] and functional peptides [8] in order to increase their versatility for biomedical applications. To functionalize graphene-based nanosheets with biologically active peptides, covalent and non-covalent methods have been used. Graphene-based nanosheets have been covalently conjugated with enzyme-sensitive peptides such as a caspase-3-cleavable peptide [9] and a protease-sensitive peptide [10] for detection of enzymes. Although non-covalent modifications are simpler processes than are covalent modifications, the direct non-covalent anchoring of a peptide onto a graphene based nanosheet can disrupt the three-dimensional conformation of the peptide, hence limiting its biological activity. [11, 12] Thus there is a need to develop a non-covalent modification technology in which peptides can bind graphene and at the same time retain their three-dimensional structures and hence functions. We aimed to carry out a simple non-covalent modification of rGO nanosheets while maintaining the biological activity of the functional peptide and biosensor.

DNA-based hydrogel that is biocompatible and biodegradable has been studied as a carrier for biomedical applications. Rolling-circle amplification (RCA) is the green method producing hydrogel composed of only DNA

material. The structure's network of RCA hydrogel is induced by the physical entanglement of long strand DNA or could be triggered based on programing of complementary sequence of the of RCA products [13, 14]. The integration of aptamers in DNA hydrogel could avoid a fast clearance in the body. The integration of aptamer into hydrogel formulation that can exert the sustain release manner would match the need for the application of aptamer in practical treatment. Several previous studies have been prepared DNA hydrogel with cross linkers which are ethylene glycol diglycidyl ether, azobenzene [15, 16].

Immunotherapy has attracted prominent investigation in cancer treatment recently. Being apart from conventional cancer therapies, such as chemotherapy, radiotherapy or surgery therapy, immunotherapy modulate and boost the antitumor activity of immune system [17]. In the pathogenesis of cancer, the out balancing of immune system caused by the upregulation of immune checkpoints, which suppress the anti-tumor function of immune cells [18]. The application of immune checkpoint inhibitors has brought cancer immunotherapy to a new stage of treatment where the target of therapy are immune cells. The expression of program death receptor-1 (PD-1) in activated T cells has been approved as the target in clinical treatment of various cancer such as melanoma, non-small cell lung cancer, head and neck squamous cell carcinoma using anti-PD1 monoclonal antibody [19]. Given the strong response to immune checkpoint blockade therapy in certain patients, the resistance to anti-PD-1 therapy using antibody has remained

concern [20]. Recently, the fast clearance of PD-1 antibody at tumor tissue due to the high expression of Fc receptors on tumor-associated macrophages have revealed a possible mechanism for resistance of this immune checkpoint inhibitors [21]. Beside the high cost of manufacturing and quality control, the humoral immune response against the antibody-based therapy still face the challenge in long-term treatment [22].

Aptamer, an oligonucleotides can bind to a specific target molecule, own the advantages that may overcome the limitation of antibody, such as thermal stability, solvent stability, low-immunogenicty, [23, 24]. Aptamer are intensively studied to catch up the application of antibody in diverse therapies. A previous study investigated PD-1 aptamer sequence that inhibits PD-1/PD-L1 interaction between cancer cells and T cells. Blockade of this interaction via PD-1 aptamer was proved to strengthen the level of immunity by recovering T cell activity both in vitro and in vivo model [25]. Despite of some advantages, aptamer encounter a fast clearance in the body. For overcoming a fast clearance problem, it need to be modified with PEG or to be delivered by some carriers [26].

CRISPR associated protein 9 (Cas9) is prokaryotic adaptive immune system for protecting host from various phages. Because of its excellent target specificity and relative easy processing procedure, Cas9 system was widely utilized for genome editing [27]. In this study, we enlarged territories of Cas9 system to drug delivery system. We constructed PD-1 aptamer hydrogel composed of two type of RCA products that contain not only the

PD-1 aptamer sequence but also the partially complementary sequence. The programed complementary sequence simultaneously play a role of cross-linker to form 3D network of hydrophilic DNA strands and of recognized sequence for the cleavage by Cas9. The combination of Cas9 and single strand guided RNA (Cas9/sgRNA) with DNA hydrogel would specifically cleave the hydrogel structure at the designed point and sustain release the functional PD-1 aptamer. In this study, the design of Cas9/PD-1 aptamer hydrogel system was characterized and evidenced the potential application in cancer immunotherapy.

2. Biomedical applications of functionalized biomaterials

Biomaterials have been studied in the biomedical fields which are therapeutic and diagnostic area for about 50 years [28]. Biocompatibility is imperative to biomaterials for utilizing as biomedical applications, which should elicit no or little immune response in organism [29]. Many candidates of biomaterials from nature and the laboratory by synthesis are commonly used with good biocompatibility. Functionalization of biomaterials is critical to maximize their suitable efficacy [30]. In terms functionalized biomaterials, graphene and DNA are widely used in biomedical applications. as listed in Table I-1.

Table I-1. Biomedical applications of GO and RCA based materials

Graphene based biomaterials			
classification	application	detail	Ref.
Biosensor	matrix for mass spectra	DNA	38
	Optical sensor	Oligonucleotides	38, 40, 41
	Electrochemical sensing	pathogen	39
		Enzymes	36, 42
		Small molecules	37, 44
anticancer therapy	Drug delivery	Chemotherapeutics	45
	Photothermal therapy	PEG-rGO,GO-AuNP	55, 56, 57, 58
RCA based biomaterials			
classification	application	detail	Ref.
Biosensor	Optical sensor	Pyrophosphate,16S rDNA	60, 65
	Electrochemical sensing	Deoxyribozyme	64
anticancer therapy	cancer cell recognition	SYL3C aptamer	61
		TD05, TE02 aptamer	67
	Nucleic acid drug delivery	CpG ODN	68, 69
		siRNA	70
	Small molecule drug delivery	Dox	62, 71

2.1. Graphene based materials

Graphene is a nanomaterials that consist of carbon, which is two dimensional hexagonal monolayers arranged sp^2-hybridized carbon atoms [31]. By graphene exfoliated with oxidation, Graphene oxide (GO) nanosheets contain some functional groups such as contain hydroxyl (-OH), epoxide (-O-) and carboxyl (-COOH) group [32]. With these functional groups, GO nanosheets are hydrophilic. Reduced from GO by heating with hydrazine, reduced GO (rGO) nanosheets are shown more crystaline graphene regions [33] and to increase hydrophobicity [34]. For these unique properties, GO was firstly used as a nanocarrier for drug delivery in 2008 [35]. Since this first application on biomedical, there are a lot of study for widespread applications.

Biosensor applications have studied with GO and rGO nanosheets [36, 37, 38, 39, 40, 41, 42]. Due to properties of GO, π-π interaction on surface of GO, Only ssDNA can bind to GO nanosheets not dsDNA. That is a reason why π-π interaction is weakened after hybridization of ssDNA to dsDNA [40, 41]. Using this characteristic, some groups have developed GO based DNA detection systems and selective fluorescence–quenching platforms [38, 40]. GO based electronic devices for detection of proteins, bacterium, and DNA have been fabricated [43]. With ultra-high surface area of GO and excellent mobility of its electron, GO and GO-based composite materials were utilized to change electrodes in the electrochemical sensor of diverse biomolecules, such as proteins, DNA and glucose, with high receptions [42,

44].

Owing to not only large surface area but also capacity of loading of drugs by physical adsorption or chemical conjugation, GO nanosheets have been attracted as novel nano-drug-carriers [45, 46, 47]. Furthermore, the reactive hydroxyl and carboxyl groups on surface facilitate GO to conjugate with various substance, such as polymers [48], biomolecules [49, 50, 51], Fe3O4 nanoparticles [52], quantum dots [53]. This strategy enables GO based biomaterials to approach for anticancer therapy with multi-functionalities, and multi-modalities.

GO based biomaterials can highly absorb visible and near-infrared (NIR) light and converse absorbed light into heat. Following this property, GO nanosheets have been widely utilized in photothermal therapy (PTT) for treating cancer [54]. PEG-coated rGO nanosheets was exploited for PTT by intravenous injection, showing powerful photothermal anticancer effect in xenograft mouse model. [55]. GO and rGO nanosheets, anchored by gold nanoparticles, were also applied for PPT [56, 57]. GO nanosheets and gold nanoparticles have shown synergistic effect on PTT at 808 nm [58].

2.1. RCA-based materials

Rolling circle amplification (RCA) is a process, consist of isothermal and enzymatic steps with unique polymerase, to prepare long single strand DNA (ssDNA) and RNA [59]. Since both DNA and RNA are biocompatible and biodegradable, RCA based materials have attracted interest to develop new

molecular technique for biomedical applications such as biosensor, cancer cell recognition and drug delivery [60, 61, 62].

With amplifying a single binding signal over thousands fold, RCA reaction is suitable for biosensor. RCA is an analytical method to detect not only other biomolecules but also nucleic acids [63]. RCA were combined with bioluminescence assay for quantification of miRNA [60]. Owing to high reproducibility of RCA, the sensor can detect a target RNA sequence, as low as 0.1 fmol, in total extracts. RCA-based sensor is capable of detecting guanosine triphosphate by kinase DNAzyme conversion [64]. For pathogenic microorganisms isothermal indicator, A surface plasmon resonance biosensor also utilized RCA technique with gold nanoparticles [65].

RCA reaction have been used to capture and isolate cancer cells by signal amplification. [66] To detect and recognize target cancer cells, a RCA based platform were developed with hairpin structured aptamer sequence [61]. To improve sensitivity and selectivity of cancer cell recognition the dual-aptamer was applicated with amplified chemiluminescence intensity signal by RCA [67].

Functional RCA-based nanotechnologies which is composed of functional sequences such as DNA aptamers have been also used for nucleic acid drug delivery [62]. CpG oligonucleotide (ODN) can be delivered as DNA nanoribbon structures by RCA reaction [68, 69]. Within DNA nanoribbon structure, CpG ODN can be protected from degradation by nuclease and

show more efficient boost immunity. Y-shaped DNA nanostructures by RCA had been designed for site-specific restriction cleavage [70]. A three- way in three hairpin loops attribute to Y-shape of DNA nanostructures, which facilitates hybridization with siRNA conjugated folic acid with complementary sequence.

RCA based materials have been studied for chemical drug delivery as well as nucleic acid drug delivery. Anticancer drug such as doxorubicin (Dox) was delivered to targeted cancer cell by a polyvalent aptamer system [62]. Dox, which can intercalated to ssDNA, was loaded to RCA product with its property. Using anti protein tyrosine kinase 7 (PTK7) aptamer sequence, DNA nanostructures were developed for anticancer therapy based on drug delivery [71]. The RCA template designed with anti-PTK7 aptamer and drug loading sites is capable of forming “DNA nanoflowers’, which is utilized both for drug delivery and PTK7 targeting.

4. Scope of the study

As fuctionalized biomaterials, GO and RCA have received tremendous attention in biomedical application field, especialy anticancer therapy, cancer diagnosis. Owing to high capacity of GO for drug loading and photothermal effect, GO have been widely utilized for cancer treatment. Many research groups have also focused on the benefits of RCA, such as biodegradability, biocompatibility and tailor-designed availability by manipulating the circular template, etc.

In chapter II, we develop a sensitive and selective rGO-based fluorescent aptasensor for IFN-γ detection. The sensitivity and selectivity of aptasensor were evaluated after treatment of IFN-γ. Finally, in order to verify applicability of the aptasensor for clinical sample analysis, we detected IFN-γ in condition of human plasma from healthy individuals. And, we develop that rGO-based fluorescent aptasensor can sensitively and selectively detect IFN-γ in presence of human plasma samples.

In chapter III, we engineered a chimeric peptide that consists of a biologically functional peptide sequence, a spacer sequence and a sequence that binds reduced graphene oxide (rGO) nanosheets in order to carry out a simple single-step non-covalent functionalization. For binding rGO, we tested a heptaphenylalanine sequence with a spacer in engineered chimeric peptides, which is containing Bu. And we reported their influence that the biological activity of the functional part of the peptide following attachment

onto rGO nanosheets.

In chapter IV, we used the precise double stranded DNA-editing function of Cas9/sgRNA to design a DNA hydrogel which can release anti-PD-1 aptamers in programmed manner. To form Cas9-edited DNA hydrogels of PD-1 aptamers, we formed DNA aptamer hydrogels using RCA methods. DNA hydrogels were crosslinked by hybridization of two types of RCA products with sgRNA target or complimentary sgRNA target sequence. Upon addition with Cas9/sgRNA, the hydrogels leaded sustained releas PD-1 DNA aptamers at injection site, enhancing activation of immune systems.

5. References

[1] Bitounis D, Ali-Boucetta H, Hong BH, Min DH, Kostarelos K. Prospects and challenges of graphene in biomedical applications. Adv. Mater. 2013;25:2258–2268

[2] Goenka S, Sant V, Sant S. J. Graphene-based nanomaterials for drug delivery and tissue engineering. Controlled Release. 2014;173:75–88.

[3] Shim G, Kim JY, Han J, Chung SW, Lee S, Byun Y, Oh YK. Reduced graphene oxide nanosheets coated with an anti-angiogenic anticancer low-molecular-weight heparin derivative for delivery of anticancer drugs. J. Controlled Release. 2014;189;80–89.

[4] Wang Y, Lee WC, Manga KK, Ang PK, Lu J, Liu YP, Lim C T, Loh KP. Fluorinated graphene for promoting neuro-induction of stem cells. Adv. Mater. 2012;24:4285–4290.

[5] Miao W, Shim G, Lee S, Oh YK. Structure-dependent photothermal anticancer effects of carbon-based photoresponsive nanomaterials. Biomaterials. 2014;35:4058–4065.

[6] Miao W, Shim G, Kang CM, Lee S, Choe YS, Choi HG, Oh YK. Cholesteryl hyaluronic acid-coated, reduced graphene oxide nanosheets for anti-cancer drug delivery. Biomaterials. 2013;34;9638–9647.

[7] Robinson JT, Tabakman SM, Liang Y, Wang H, Sanchez Casalongue H, Vinh D, Dai H. Ultrasmall reduced graphene oxide with high near-infrared absorbance for photothermal therapy. J. Am. Chem. Soc. 2011;133:6825–6831.

[8] Wang E, Desai MS, Lee SW. Light-controlled graphene-elastin composite hydrogel actuators. Nano Lett. 2013;13:2826–2830.

[9] Wang H, Zhang Q, Chu X, Chen T, Ge J, Yu R, Angew. Graphene oxide-peptide conjugate as an intracellular protease sensor for caspase-3 activation imaging in live cells. Chem. Int. Ed. Engl.

2011;50:7065–7069.

[10] Kwak SY, Yang JK, Jeon SJ, Kim HI, Yim J, Kang H, Kyeong S., Lee YS, Kim JH. Graphene oxide-encoded Ag nanoshells with single-particles. Adv. Funct. Mater. 2014;24:5119–5128.

[11] Alava T, Mann JA, Th´eodore CC, Benitez JJ, Dichtel WR, Parpia J M, Craighead H G. Control of the graphene-protein interface is required to preserve adsorbed protein function. Anal. Chem. 2013;85:2754–2759.

[12] Mann JA, Dichtel WR. Improving the binding characteristics of tripodal compounds on single layer graphene. ACS Nano. 2013;7:7193–7199.

[13] Zhang X, Chen J, Liu H, Zhang S. Quartz crystal microbalance detection of protein amplified by nicked circling, rolling circle amplification and biocatalytic precipitation. Biosens Bioelectron. 2014; 65C:341-345.

[14] Ma Y, Zheng H, Wang C, Yan Q, Chao J, Fan C, Xiao SJ. RCA strands as scaffolds to create nanoscale shapes by a few staple strands. J Am Chem Soc. 2013; 135(8):2959-2962

[15] Wang F, Willner B, Willner I. DNA nanotechnology with one-dimensional self-assembled nanostructures. Curr Opin Biotechnol. 2013; 24(4):562-574.

[16] Qi H, Ghodousi M, Du Y, Grun C, Bae H, Yin P, Khademhosseini A. DNA-directed self-assembly of shape-controlled hydrogels. Nat Commun. 2013; 4:2275.

[17] Topalian SL, Drake CG, Pardoll DM. Immune checkpoint blockade: a common denominator approach to cancer therapy. Cancer Cell. 2015;27:450-461.

[18] Sun C, Mezzadra R, Schumacher TN. Regulation and function of the PD-L1 checkpoint. Immunity. 2018:48:434-452.

[19] Simon S. Labarriere N, PD-1 expression on tumor-specific T cells:

Friend or foe for immunotherapy?. Oncoimmunology. 2017;7: e1364828.

[20] Spranger S, Spaapen RM, Zha Y, Williams J, Meng Y, Ha TT, Gajewski TF. Up-regulation of PD-L1, IDO, and T(regs) in the melanoma tumor microenvironment is driven by CD8(+) T cells. Sci. Transl. Med. 2013;5:200ra116.

[21] Hui E, Cheung J, Zhu J, Su X, Taylor MJ, Wallweber HA, Sasmal, DK, Huang J, Kim JM, Mellman I, Vale RD. T cell costimulatory receptor CD28 is a primary target for PD-1-mediated inhibition. Science. 2017; 355:1428-1433.

[22] Tumeh PC, Harview CL, Yearley JH, Shintaku IP, Taylor EJ, Robert, L, Chmielowski B, Spasic M, Henry G, Ciobanu V, West AN, Carmona M, Kivork C, Seja E, Cherry G, Gutierrez AJ, Grogan TR, Mateus C, Tomasic G, Glaspy JA, Emerson RO, Robins H, Pierce RH, Elashoff DA, Robert C, Ribas A. PD-1 blockade induces responses by inhibiting adaptive immune resistance. Nature. 2014; 515:568-571.

[23] Nozari A. Berezovski MV. Aptamers for CD antigens: from cell profiling to activity modulation. Mol. Ther. Nucleic Acids. 2017;6: 29-44.

[24] Keefe AD, Pai S, Ellington A. Aptamers as therapeutics. Nat. Rev. Drug Discov. 2010;9(7):537-550.

[25] Prodeus A, Abdul-Wahid A, Fischer NW, Huang EH, Cydzik M, Gariepy J. Targeting the PD-1/PD-L1 immune evasion axis with DNA aptamers as a novel therapeutic strategy for the treatment of disseminated cancers. Mol. Ther. Nucleic Acids. 2015; 4:e237.

[26] Lao YH, Phua KK, Leong KW. Aptamer nanomedicine for cancer therapeutics: barriers and potential for translation. ACS Nano. 2015; 9(3):2235-2254.

[27] Wang C, Sun W., Wright G, Wang AZ, and Gu Z. Inflammation-

triggered cancer immunotherapy by programmed delivery of CpG and anti-PD1 antibody. Adv. Mater. 2016;28(40):8912-8920.

[28] Vert M, Doi Y, Hellwich KH, Hess M, Hodge P, Kubisa P, Rinaudo M, Schué FO. Terminology for biorelated polymers and applications. Pure and Applied Chemistry. 2012;84(2):377

[29] Rukmani S, Brenton C, Andrew RCameron, Daniel JK, Fergal JO. Material stiffness influences the polarization state, function and migration mode of macrophages. Acta Biomaterialia. 2019;89:47–59

[30] Nikolova, Chavali. Recent advances in biomaterials for 3D scaffolds: A review. Bioact Mater. 2019;4:271-292.

[31] Geim AK. Graphene: status and prospects. Science 2009;324:1530-1534

[32] Park S, An J, Jung I, Piner RD, An SJ, Li X, Velamakanni A, Ruoff RS. Colloidal suspensions of highly reduced graphene oxide in a wide variety of organic solvents. Nano Lett 2009;9:1593-1597.

[33] Robinson JT, Tabakman SM, Liang Y, Wang H, Casalongue HS, Vinh D, Dai H. Ultrasmall reduced graphene oxide with high near-infrared absorbance for photothermal therapy. J Am Chem Soc 2011:133:6825-6831.

[34] Kim J, Kim F, Huang J. Seeing graphene-based sheets. Mat Today 2010;12:28−38.

[35] Liu Z, Robinson JT, Sun X, Dai H. PEGylated nanographene oxide for delivery of water-insoluble cancer drugs. J Am Chem Soc 2008;130:10876-10877.

[36] Shan CS, Yang HF, Song JF, Han DX, Ivaska A, Niu L. Direct electrochemistry of glucose oxidase and biosensing for glucose based on graphene. Anal Chem 2009;81:2378–2382.

[37] Song YJ, Qu KG, Zhao C, Ren JS, Qu XG. Graphene oxide: intrinsic peroxidase catalytic activity and its application to glucose detection. Adv Mater 2010;22:2206–2210.

[38] Tang LAL, Wang JZ, Loh KP. Graphene-based SELDI probe with ultrahigh extraction and sensitivity for DNA oligomer. J Am Chem Soc .2010;132:10976–10977.

[39] Wang Y, Li ZH, Hu DH, Lin CT, Li JH, Lin YH. Aptamer/graphene oxide nanocomplex for in situ molecular probing in living cells. J Am Chem Soc. 2010;132:9274–9276.

[40] Jang HJ Kim YK Kwon HM Yeo WS Kim DE Min DH. A graphene-based platform for the assay of duplex-DNA unwinding by helicase. Angew. Chem. Int. Ed. 2010;49:5703–5707.

[41] Lu CH, Zhu CL, Li J, Liu JJ, Chen X, Yang HH. Using graphene to protect DNA from cleavage during cellular delivery. Chem. Commun. 2010;46:3116–3168.

[42] Zeng QO, Cheng JS, Tang LH. Self-assembled graphene–enzyme hierarchical nanostructures for electrochemical biosensing. Adv. Funct. Mater. 2010;20:3366–3372.

[43] Mohanty N, Berry V. Graphene-based single-bacterium resolution biodevice and DNA transistor: interfacing graphene derivatives with nanoscale and microscale biocomponents. Nano Lett. 2008;8:4469–4476.

[44] Lu CH, Yang HH, Zhu CL, Chen X, Chen GN. A graphene platform for sensing biomolecules. Angew. Chem. Int. Ed. 2009;48:4785–4787.

[45] Wu J, Wang YS, Yang XY, Liu YY, Yang JR, Yang R, Zhang N. Graphene oxide used as a carrier for adriamycin can reverse drug resistance in breast cancer cells. Nanotechnology. 2012;23:355101.

[46] Hu H, Yu J, Li Y, Zhao J, Dong H. Engineering of a novel pluoronic F127/graphene nanohybrid for pH responsive drug delivery. J Biomed. Mat. Res. A 2012;100:141-148.

[47] Wen H, Dong C, Dong H, Shen A, Xia W, Cai X, Song Y, Li X, Li Y, Shi D. Engineered redox-responsive PEG detachment mechanism in

PEGyalted nano-graphene oxide for intracellular drug delivery. Small. 2012;8:760-769.

[48] Shan CS, Yang HF, Han DX. Zhang QX, Ivaska A, Niu L. Water-soluble graphene covalently functionalized by biocompatible poly-L-lysine. Langmuir. 2009;25:12030-12033.

[49] Sun XM, Liu Z, Welsher K. Nano-graphene oxide for cellular imaging and drug delivery. Nano Res. 2008;1:203-212.

[50] Lei HZ, Mi LJ, Zhou XJ. Chen JJ, Hu J, Guo SW, Zhang Y. Adsorption of double-stranded DNA to graphene oxide preventing enzymatic digestion. Nanoscale 2011;3:3888-3892.

[51] Zhang JL, Zhang F, Yang HJ. Huang XL, Liu H, Zhang JY, Guo SW. Graphene oxide as a matrix for enzyme immobilization. Langmuir. 2010;2:6083-6085.

[52] Chen WH, Yi PW, Zhang Y. Composites of aminodextran-coated Fe3O4 nanoparticles and graphene oxide for cellular magnetic resonance imaging. ACS Appl. Mater. Interfaces 2011;3:4085-91.

[53] Shen JF, Shi M, Li N, Yan B, Ma HW, Hu YZ, Ye MX. Facile synthesis and application of Ag-chemically converted graphene nanocomposite. Nano Res. 2010;3:339-349.

[54] Kam NWS, O'Cornell M, Wisdom JA, Dai H. Carbon nanotubes as multifunctional biological transporters and near-infrared agents for selective cancer cell destruction. Proc. Natl. Acad. Sci. 2005,102:11600-11605.

[55] Yang K, Wan J, Zhang S, Tian B, Zhang Y, Liu Z. The influence of surface chemistry and size of nanoscale graphene oxide on photothermal therapy of cancer using ultra-low laser power. Biomaterials. 2012;33:2206-2214.

[56] Zedan AF, Moussa S, Terner J, Atkinson G, El-Shall, MS. Ultrasmall gold nanoparticles anchored to graphene and enhanced photothermal effects by laser irradiation of gold nanostructures in graphene oxide

solutions. ACS Nano 2013;7:627-636.

[57] Lim DK, Barhoumi A, Wylie, RG, Reznor G, Langer RS. Kohane DS.Enhanced photothermal effect of plasmonic nanoparticles coated with reduced graphene oxide. Nano Lett 2013;13:4075-4079.

[58] Zedan AF, Moussa S, Terner J, Atkinson G, El-Shall, MS. Ultrasmall gold nanoparticles anchored to graphene and enhanced photothermal effects by laser irradiation of gold nanostructures in graphene oxide solutions. ACS Nano. 2013,7:627-636.

[59] Liu M, Song J, Shuang S, Dong C, Brennan JD, Li Y. A graphene-based biosensing platform based on the release of DNA probes and rolling circle amplification. ACS Nano. 2014; 8(6):5564-5573.

[60] Mashimo Y, Mie M, Suzuki S, Kobatake E. Detection of small RNA molecules by a combination of branched rolling circle amplification and bioluminescent pyrophosphate assay. Anal Bioanal Chem. 2011; 401(1): 221-227.

[61] Sheng Q, Cheng N, Bai W, Zheng J. Ultrasensitive electrochemical detection of breast cancer cells based on DNA-rolling-circle-amplification-directed enzyme-catalyzed polymerization. Chem. Commun. 2015; 51(11):2114-2117.

[62] Zhang Z, Ali MM, Eckert MA, Kang DK, Chen YY, Sender LS, Fruman DA, Zhao W. A polyvalent aptamer system for targeted drug delivery.Biomaterials. 2013; 34(37):9728-9735.

[63] Kobori T, Takahashi H. Expanding possibilities of rolling circle amplification as a biosensing platform. Anal Sci. 2014; 30(1):59-64.

[64] McManus SA, Li Y. Turning a kinase deoxyribozyme into a sensor. J Am Chem Soc. 2013; 135(19):7181-7189.

[65] Shi D, Huang J, Chuai Z, Chen D, Zhu X, Wang H, Peng J, Wu H, Huang Q, Fu W. Isothermal and rapid detection of pathogenic microorganisms using a nano-rolling circle amplification-surface plasmon resonance biosensor. Biosens Bioelectron. 2014;62:280-287.

[66] Zhou G, Lin M, Song P, Chen X, Chao J, Wang L, Huang Q, Huang W, Fan C, Zuo X. Multivalent capture and detection of cancer cells with DNA nanostructured biosensors and multibranched hybridization chain reaction amplification. Anal. Chem. 2014; 86(15):7843-7848.

[67] Bi S, Ji B, Zhang Z, Zhang S. A chemiluminescence imaging array for the detection of cancer cells by dual-aptamer recognition and bio-bar-code nanoprobe-based rolling circle amplification. Chem .Commun. 2013; 49(33):3452-3454.

[68] Ouyang X, Li J, Liu H, Zhao B, Yan J, Ma Y, Xiao S, Song S, Huang Q, Chao J, Fan C. Rolling circle amplification-based DNA origami nanostructrures for intracellular delivery of immunostimulatory drugs.Small. 2013; 9(18):3082-3087.

[69] Ouyang X, Li J, Liu H, Zhao B, Yan J, He D, Fan C, Chao J. Self-assembly of DNA-based drug delivery nanocarriers with rolling circle amplification. Methods. 2014; 67(2):198-204.

[70] Zheng HN, Ma YZ, Xiao SJ. Periodical assembly of repetitive RNA sequences synthesized by rolling circle transcription with short DNA staple strands to RNA-DNA hybrid nanowires. Chem. Commun. 2014; 50(17):2100-2103.

[71] Hu R, Zhang X, Zhao Z, Zhu G, Chen T, Fu T, Tan W. DNA nanoflowers for multiplexed cellular imaging and traceable targeted drug delivery. Angew. Chem. Int. Ed. Engl. 2014; 53(23):5821-5826.

Chapter II

Double stranded aptamer-anchored reduced graphene oxide as target-specific nano detector

1. Introduction

Aptamers, also known as chemical antibodies, are short single-stranded DNA (ssDNA) or RNA oligonucleotides that can bind a wide range of targets, including proteins [1], DNA [2,3] small molecules [4], and metal ions [5] with high specificity and affinity. Since aptamers offer advantages such as high thermal stability, ease of chemical modification, and inclusion of surface binding or sensing moieties compared to antibodies [6,7]. There has been increased interest in development of aptasensors based on fluorescence, surface-enhanced Raman spectroscopy, microgravimetry, and electrochemistry.

Among such, detection by fluorescence change is an attractive way to develop aptasensors owing to the features such as high sensitivity, reproducibility, and facile operation [8,9]. Conventional aptasensor detects fluorescence resonance energy transfer signals when the ligand-induced conformational changes of fluorophore and quencher labeled-aptamers occur. However, the sensitivity of such system is largely influenced considerably by the length of quencher labeled DNA and temperature [10]. Thus, there is still a need for the development of new platform that can detect target molecules, selectively and sensitively.

Graphene, a two-dimensional nanosheet, has recently received considerable attention due to its remarkable electronic, mechanical, and

thermal properties [11]. Reduced graphene oxide (rGO) can be chemically synthesized by placing graphene oxide (GO) in a solution of hydrazine [12]. Since rGO contains more crystalline graphene regions on the sheet compared to GO, the stronger adsorption of aptamer on rGO surface through hydrophobic and π-π stacking interactions between the ring structures in the nucleobases occurs [13]. Moreover, rGO can act as a more effective distance-dependent fluorescence quencher than GO or graphene [14]. With combined features of high fluorescence quenching efficiency and superb ssDNA adsorption ability, rGO is applicable to detection mechanisms.

Cytokines are proteins used for cell signaling and often secreted by immune cells in response to various pathogens [15]. The monitoring secreted cytokines can provide diagnostic information about various infectious diseases in patients. For example, in human immunodeficiency virus (HIV) infected patients, T-helper and cytotoxic T-lymphocytes vigorously produce the cytokine protein such as interferon-g (IFN-γ), resulting in low viremia and slow progression of the disease [16,17]. It is therefore important to detect cytokine levels for clinical diagnostic purposes. Conventional antibody-based immunoassay, such as enzyme-linked immunosorbent assay, is common methods for detecting and quantification secreted cytokines. Although immunoassays is sensitive and specific to the target protein, it requires multiple washing steps and the use of expensive reagents [18]. Moreover, low stability of monoclonal antibody causes reduction of affinity between antibody and antigen. The development of a

new assay system that saves time and reduces costs would thus be desirable.

In this study, we designed a double-stranded, dual-anchored, fluorescent (FAM-labeled) aptamer on rGO nanosheets for quantitation of target protein in biological samples. To prevent nonspecific quenching of fluorescent aptamer upon interaction with rGO, we hybridized the fluorescent aptamer with a complementary sequence to form double strands. To fortify the anchoring on rGO, we labeled the double-stranded fluorescent aptamer with two anchoring moieties. As a model target protein specific for the aptamer, IFN-γ was used.

2. Materials and methods

2.1 Chemicals and DNA sequences

The following chemicals are purchased from Sigma-Aldrich (St. Louis, MO, USA): graphite powders, sulfuric acid (H_2SO_4), potassium permanganate ($KMnO_4$), sodium nitrate ($NaNO_3$), hydrogen peroxide (H_2O_2), Hydrochloric acid (HCl), and hydrazine monohydrate. Ammonia solution was purchased from JUNSEI (Tokyo, Japan). Recombinant human IFN-γ, Interleukin-2 (IL-2), and Tumor Necrosis Factor-α were obtained from R&D Systems, Inc. (Minneapolis, MN). Plasma samples from 5 healthy human subjects were obtained from SCIPAC Ltd (Kent, UK). All of the DNA oligonucleotides were synthesized and purified by Bioneer Corporation (Daejeon, Korea). The FAM- and/or BHQ1-labeled DNA sequences are listed in Table II-1.

Table II- 1. Sequence information for aptasensor

Length (bp)	Sequences
6	5’-FAM-GGG GTT-BHQ1-3’
	5’-BHQ1-AAC CCC-3
16	5’-FAM-GGG GTT GGT TGT GTT G-BHQ1-3
	5’-BHQ1-CAA CAC AAC CAA CCC C-3’
26	5’-FAM-**GGG GTT GGT TGT GTT GGG TGT TGT GT**-BHQ1-3’
	5’-BHQ1-ACA CAA CAC CCA ACA CAA CCA ACC CC-3’
36	5’-FAM-AT**G GGG TTG GTT GTG TTG GGT GTT GT**G TTG AGC GCT-BHQ1-3’
	5’-BHQ1-AGC GCT CAA CAC AAC ACC CAA CAC AAC CAA CCC CAT-3’
46	5’-FAM-AT**G GGG TTG GTT GTG TTG GGT GTT GTG T**TG AGC GCT GTT GAG CGC T-BHQ1-3’
	5’-BHQ1-AGC GCT CAA CAG CGC TCA ACA CAA CAC CCA ACA CAA CCA ACC CCA T-3’

Underline and boldface latters indicate IFN-γ recognizing aptamer sequences.

2.2. Synthesis of rGO nanosheets

GO was prepared from graphite powder following a modified Hummer's method [12]. Briefly, graphite powder (0.5 g; Sigma Aldrich, St. Louis, MO, USA) was added to cold H2SO4 (23 ml). While this mixture was gradually stirred on ice, KMnO4 (3 g) and NaNO3 (0.5 g) were added slowly. The resulting mixture was further stirred for 1 h at 35 ℃. Subsequently, 46 ml of triple-distilled water (TDW) was added and the mixture was incubated at 90 ℃ for 1 h. The reaction was halted by adding 140 ml of TDW and 10 ml of 30% H_2O_2. The reaction product underwent repeated centrifugation to wash and purify the product; first with an aqueous 5% HCl solution, and then with TDW (three times). Finally, the product was suspended in TDW and sonicated for 2 h to exfoliate the GO layers into GO nanosheets. The unexfoliated GO layers were removed by centrifugation at 1600 x g for 10 min. The supernatant containing GO nanosheets was collected and an extruder (Northern Lipid, British Columbia, Canada) was used to filter it through 0.2-μm polycarbonate membrane filters (Millipore Corp., Billerica, MA, USA).

GO nanosheets were further reduced to make rGO nanosheets according to a method presented by Li and colleagues [19], with slight modification. Briefly, 2.0 ml of homogeneously dispersed GO nanosheet solution was mixed with 8.0 ml of TDW, 0.5 ml of ammonia solution (28 wt% in water; Junsei Chemical Co., Tokyo, Japan), and 5.0 ml of hydrazine monohydrate (64% in water). The resultant mixture was stirred in a water bath (80 ^{o}C) for

10 min. Subsequently, the mixture was removed from a water bath and allowed to cool down to room temperature. To remove the excess hydrazine and ammonia, the mixture was dialyzed (MWCO 100K; Spectrum Laboratories, Inc., Rancho Dominguez, CA, USA) with TDW for 2 days with 4 renewals of TDW over 12 h. interval. The obtained rGO nanosheets dispersed in TDW was stored at 4 ^{o}C until use. The final concentration of the prepared rGO was 1 mg/ml.

2.3. Anchoring of target protein-specific fluorescent aptamers onto rGO nanosheets

Double-stranded aptamer structures dually anchored with Black Hole Quencher-1 (BHQ1) were designed for perpendicular anchoring of IFN-γ specific fluorescent ssDNA aptamers (36 bp) to rGO nanosheets (Fig. II -3A). Single-stranded IFN-γ specific fluorescent DNA aptamers (ssAptamer, 25 mg/ml, Bioneer, Daejeon, South Korea) containing FAM dye at the 5'-end and BHQ1 at the 3'-end were hybridized in hybridization buffer (10 mM TriseHCl, 1 mM EDTA, 100 mM NaCl, pH 8.0) with complementary ssDNA oligonucleotides singly labeled with BHQ1 (25 mg/ml). Double-stranded fluorescent aptamers (dsAptamer) were formed by heating the solution containing ssAptamers of various lengths and complementary oligomers to 95 C for 5 min and slowly cooling to 30 ^{o}C to allow hybridization. Doublestranded, dual-anchored, fluorescent aptamers (dsDA-Aptamer; 50 mg/ml) were immobilized onto the rGO surfaces by adding 10

mg/ml of rGO to the resultant solution. In some experiments, ssAptamers were hybridized with complementary DNA sequences with or without BHQ1, to which 10 mg/ml of rGO was added. The mixture was vortexed vigorously and incubated at room temperature for 30 min to induce formation of dsDA-Aptamers on rGO nanosheets (DAGO). The solution was centrifuged at 6000 g for 2 min to remove excess, unattached aptamers. The supernatant was discarded and the remaining pellet was suspended in hybridization buffer (200 ml).

2.3. Target protein sensitivity and specificity test

The sensitivity of DAGO for its target protein was evaluated by incubating 10 mg/ ml of DAGO with different concentrations of human IFN-γ (R&D Systems, Inc., Minneapolis, MN, USA) ranging from 100 pg/ml to 10 mg/ml. Specificity was demonstrated by challenging DAGO with 10 mg/ml of human tumor necrosis factor-a (TNF- a; R&D Systems), interleukin-2 (IL-2; R&D Systems), or the analyte of interest (1 mg/ml of IFN-γ). After incubating for 3 min at room temperature, the solution was centrifuged at 6000 g for 2 min to remove any excess, unreacted materials and the remaining pellet was resuspended in hybridization buffer (200 ml). The binding of IFN-γ to DAGO was determined by exciting at a wavelength of 485 nm and measuring fluorescence intensity at an emission wavelength of 520 nm using a spectrophotometer (Molecular Devices, Sunnyvale, CA,

USA)

2.4. Assay of target protein in human serum

In order to detect IFN-γ in human plasma, the samples from 5 healthy individuals were spiked with various concentrations of IFN-γ. The spiked plasma samples were applied to the DF-aptasensor. Upon addition, the final concentration of IFN-γ came to be ranging from 100 pg/ml to 10 μg/ml. The solution was vortexed vigorously and allowed to interact for 30 min. After incubation, it was centrifuged at 8000 rpm for 10 min. The precipitated was resuspended in hybridization buffer (200 μl).

2.5. DAGO-based detection of target protein in human patient samples

DAGO was used to detect IFN-γ in serum samples from HIV-positive patients. Solutions were prepared by adding DAGO (10 mg/ml) to 120 ml of phosphate-buffered saline (PBS) and 80 ml of serum samples from healthy individuals (Scipak Ltd, Kent, UK) or HIV-positive patients (Korea National Public Health Institute, Osong, Republic of Korea). Incubation and processing of samples, and determination of fluorescence intensity, were as described above. In some experiments, Quantitkine ELISA human IFN-γ (R&D Systems) was used to detect IFN-γ in serum samples from HIV-positive patients

2.6. Statistics

Analysis of variance (ANOVA) with Student-Newman-Keuls post-hoc test was used for statistical evaluation of experimental data. All statistical analyses were done using SigmaStat software (version 3.5, Systat Software, Richmond, CA, USA); a pvalue < 0.05 was considered significant.

3. Results

3.1. Effect of the double-stranded structure of fluorescent aptamers on rGO-dependent fluorescence quenching

The double-stranded structure of fluorescent aptamers played a major role in preventing the severe quenching of fluorescence intensity by the associated rGO nanosheets. To test the effect of the double-stranded structure of FAM-labeled, fluorescent aptamers on degree of fluorescence quenching by rGO, we anchored ssAptamers or dsAptamers on rGO nanosheets (Fig. II -1A) and compared fluorescence intensity. The fluorescence intensity of rGO alone was significantly quenched upon loading onto rGO nanosheets. In contrast, dsAptamers showed higher retention of fluorescence after complexation on rGO. The fluorescence intensity of dsAptamers on rGO was 7.3-fold higher than that of ssAptamers on rGO (Fig. II -1B).

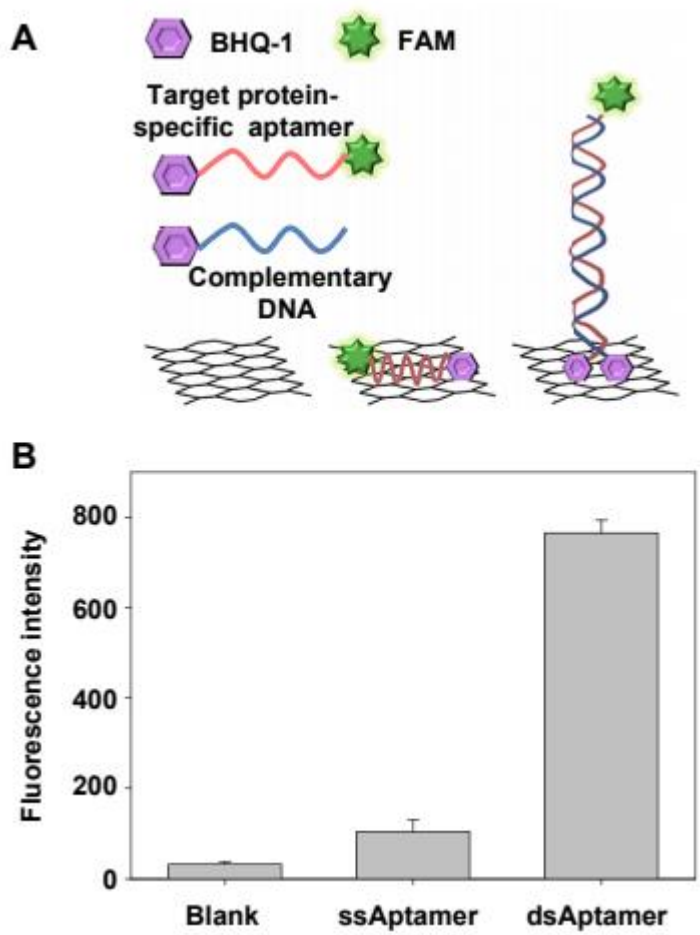

Fig. II-1. Fluorescence intensity of ssAptamers and dsAptamers on rGO

(A) Schematic representation of ssAptamers and dsAptamers anchored on a rGO nanosheet. (B) Fluorescence intensities of rGO blank, ssAptamers on rGO, and dsAptamers on rGO were determined at an excitation wavelength of 485 nm and an emission wavelength of 520 nm (n = 4).

3.2. Effect of the number of anchoring moieties on dsAptamers

For the proposed aptamer-based nano detectors to function as envisioned, dsAptamers must be able to firmly attach to rGO surfaces without a loss of fluorescence. To this end, we formed dsAptamers containing 0, 1, or 2 BHQ1 anchoring moieties and tested their retention of fluorescence upon anchoring to rGO. As illustrated in Fig. II -2A, dsAptamers containing 1 or 2 BHQ1 moieties were prepared by hybridizing BHQ1-containing ssAptamers with a complementary strand containing or lacking BHQ1. Hybridization of ssAptamers without BHQ1 with a complementary strand without BHQ1 yielded dsAptamers with no BHQ1 moiety. Upon loading onto rGO, dsAptamers with 0 or 1 BHQ1 anchoring moiety failed to show a distinctive recovery of fluorescence. In contrast, dsAptamers containing 2 BHQ1 anchoring moieties (dsDAAptamers) retained their fluorescence intensity upon binding to rGO (Fig. II -2B). Thus, a critical element in the proposed aptamerbased nano detectors design is the presence of dual anchoring moieties

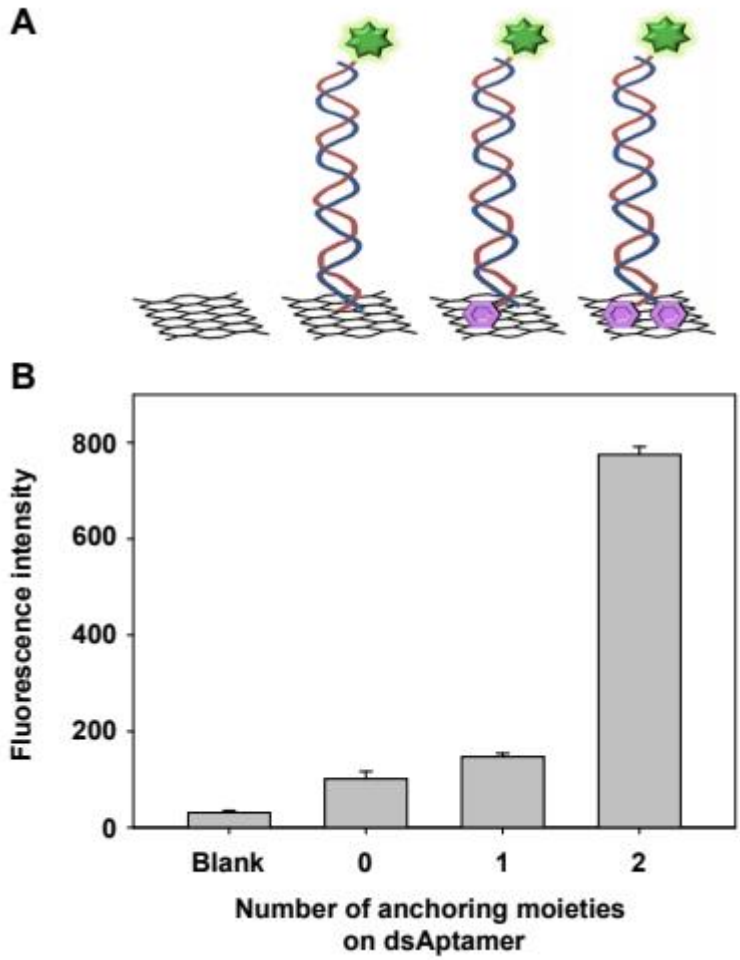

Fig. II-2. Fluorescence intensity on rGO nanosheets of dsAptamers containing varying numbers of BHQ1 anchoring moieties

(A) Illustration of dsAptamers containing 0, 1, or 2 BHQ1 anchoring moieties attached to rGO. (B) dsAptamers differing in the number of anchoring moieties were incubated for 30 min with rGO. After removal of unattached dsAptamers, the fluorescence intensity of each dsAptamer on rGO was measured at an emission wavelength of 520 nm (n = 4).

3.3. Detection of target protein using DAGO

Based on the results shown in Figs. II -1B and II -2B, a dsDA-Aptamer on rGO nanosheets, designated DAGO, was chosen for subsequent experiments. DAGO was constructed by hybridizing an ssAptamer (shown in red) possessing a FAM on the 5'-end and a BHQ1 on 3'-end with a complementary oligomer (shown in blue) containing a BHQ1-modified 5'-end. In application, DAGO monitors specific binding to its target, in this case IFN-γ, a model protein, by converting from an unbound, fluorescent state ("on") to a target-bound, fluorescence-quenched state ("off"). This is presented schematically in Fig. II -3A, which shows that as IFN-γ approaches and interacts with the IFN-γ specific,fluorescent dsDA-Aptamer, the aptamer strand binds the target protein IFN-γ, which effectively displaces the double-stranded structure into two single strands. As a consequence, the two denatured strands, together with the fluorophore, become proximate to the rGO surface. The loss of distance between the fluorophore and the rGO surface due to IFN-g binding quenches the fluorophore, result in an "off" signal. To evaluate the displacement of dsDA-Aptamer by IFN-γ, we measured the fluorescence emission intensity of FAM from dsDA-Aptamers attached to rGO before and after treatment with IFN-γ. rGO alone in buffer was used as a blank. As shown in Fig. II -3B, the fluorescent intensity of DAGO decreased by 2.8-fold following exposure to 1 mg/ml of IFN-γ.

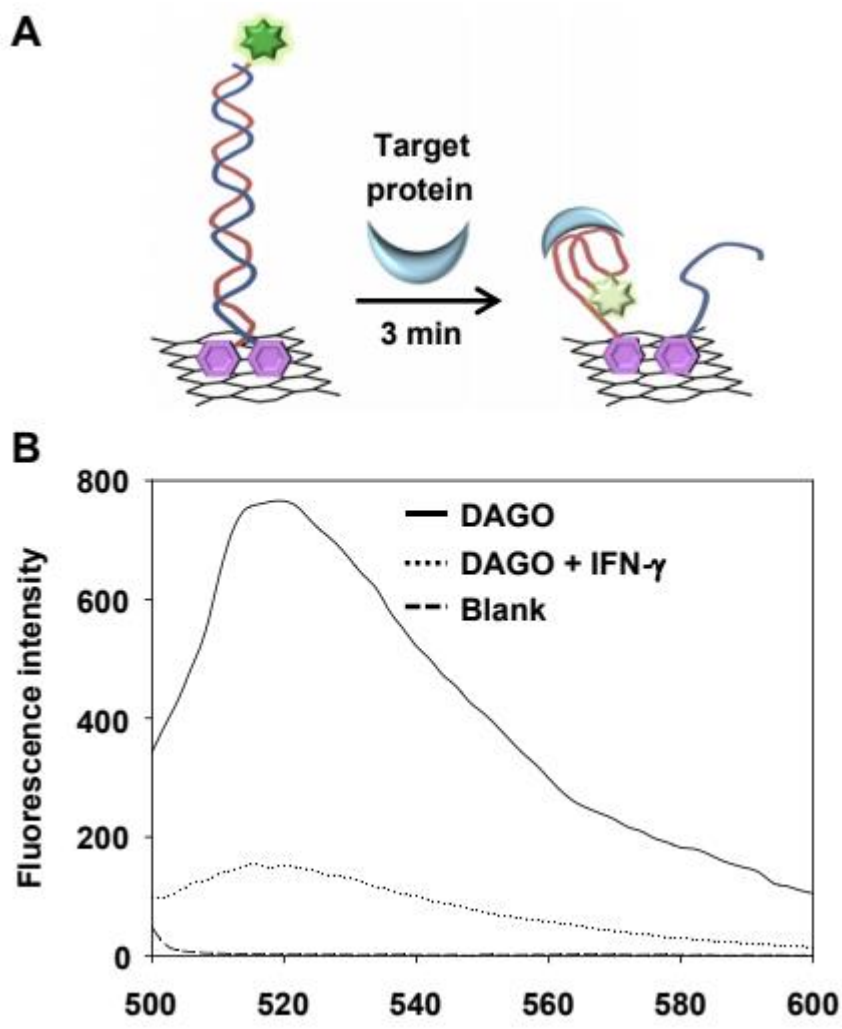

Fig. II-3. Rapid changes in fluorescence intensity of DAGO in the presence of target protein

(A) Schematic illustration of the fluorescence assay for target protein detection using DAGO. (B) DAGO (10 mg/ml) was incubated for 3 min with 1 mg/ml of a model target protein, IFN-γ. After centrifugation, the pellets were resuspended and the fluorescence intensity was measured over emission wavelengths of 500-600 nm.

3.4. Sensitivity of DAGO for target protein in buffer and human serum

To evaluate the utility of the proposed aptamer-based nanodetectors as a quantification method for target proteins under physiological conditions, we incubated DAGO with samples of buffer or human serum spiked with different concentrations of IFN-γ. As shown in Fig. II -5a, the change in the fluorescence signal of DAGO upon binding IFN-γ in buffer was linear from 100 pg/ml to 10 mg/ml. The regression coefficient of the trend-line equation was 0.9882 (Fig. II -4A). Similar to IFN-γ in buffer, IFN-γ in human serum exhibited fluorescence intensity changes that were linear from 100 pg/ml to 10 mg/ml, with a regression coefficient of 0.9838 (Fig. II -4B).

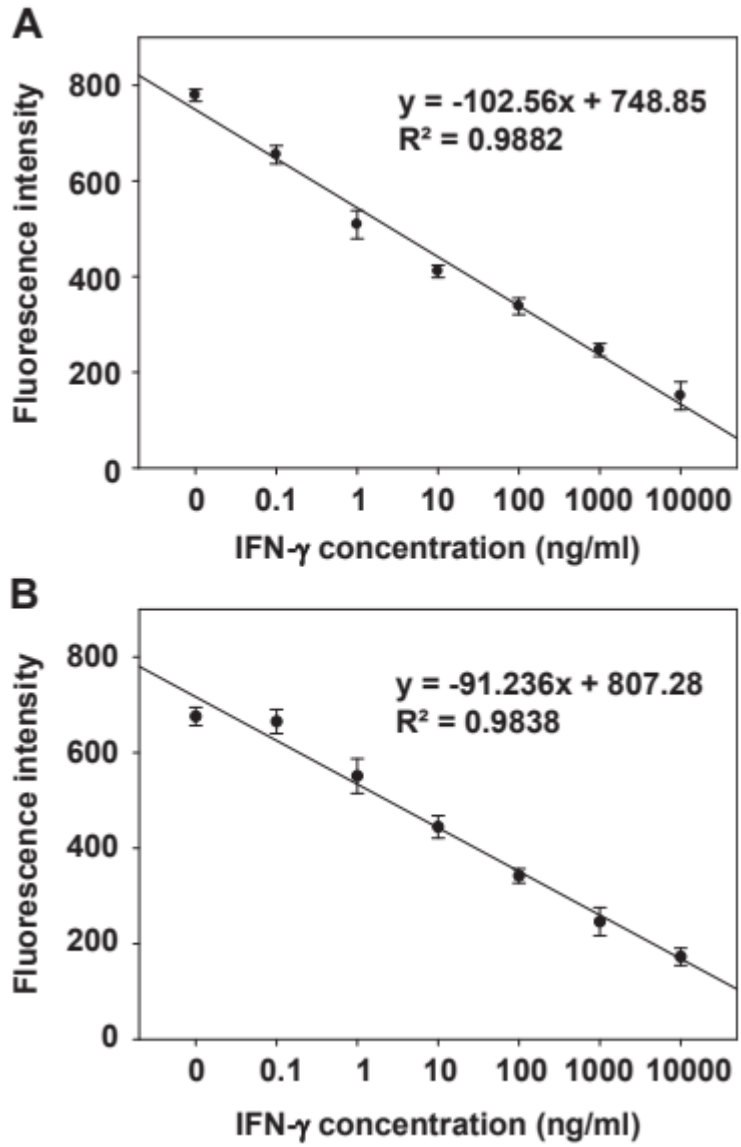

Figure II-4. Standard curves of target protein by DAGO in PBS and human serum

DAGO (10 mg/ml) was incubated for 3 min with PBS (A) or healthy human serum (B) spiked with different concentrations of IFN-γ. After incubation, the mixture was centrifuged for 2 min and the resuspended pellets were spectrophotometrically measured at an emission wavelength of 520 nm (n = 5)

3.6. Selectivity of DAGO for target protein

DAGO exhibited specificity for its target model protein, IFN-γ. To test the specificity of DAGO, we measured the degree of fluorescence intensity change after challenge with target or non-target proteins (Fig. II -5). After treatment of DAGO with 10 mg/ml of IL-2 or TNF-a, there was no apparent change in fluorescence. In contrast, a significant change in fluorescence intensity was observed after treatment of DAGO with 1 mg/ml of IFN-γ.

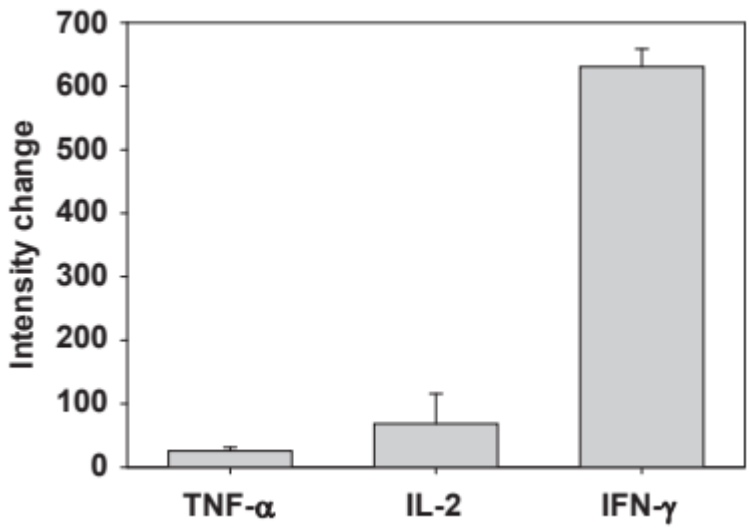

Figure II-5. Changes in the fluorescence intensity of target protein-specific aptamer-anchored DAGO in response to different proteins

DAGO (10 mg/ml) was incubated for 3 min with the target protein, IFN-γ 1 mg/ml, or non-target proteins such as IL-2 (10 mg/ ml) and TNF-a (10 mg/ml) in PBS. After incubation, the mixture was centrifuged and the resuspended pellets were spectrophotometrically measured at an emission wavelength of 520 nm (n = 4).

3.6. DAGO-based detection of target protein in patient samples

For clinical application of this system, we investigated the ability of DAGO to detect target protein in patient serum samples. Upon addition of healthy human serum samples to DAGO, there was little change in fluorescence intensity (Fig. II -6A). In contrast, the addition of HIV-positive human serum samples (n = 5) resulted in a significant change in the fluorescence intensity of DAGO. The concentrations of IFN-γ in all HIV-positive patient samples were quantified by reference to the standard curve prepared from IFN-γ spiked human serum samples and were determined to range from 330 to 550 ng/ml. Similarly, the values obtained for HIV-positive human serum samples using ELISA analysis (Fig. II -6B) were in the range of 360-520 ng/m

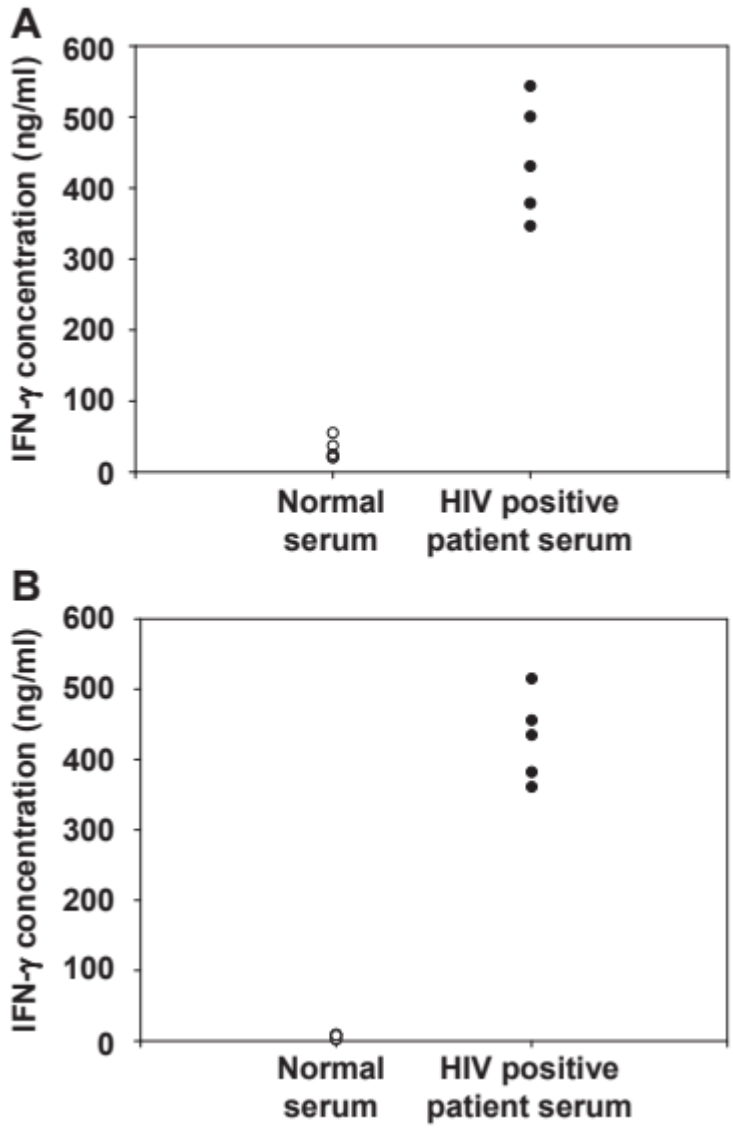

Fig. II-6. Quantification of target protein levels in patient serum samples

(A) DAGO (10 mg/ml) was incubated for 3 min with serum samples from normal or HIV-positive patients. After incubation, the mixture was centrifuged and the resuspended pellets were spectrophotometrically measured at an emission wavelength of 520 nm. The concentration of IFN-γ was calculated from fluorescence intensity changes by reference to a standard curve (n = 5). (B) The same serum samples from normal or HIV positive patients analyzed with the IFN-γ ELISA kit

4. Discussion

Here, we report the development of a dsDA-Aptamer and rGO based nano detectors, termed DAGO, that is capable of detection and quantification of IFN-γ in human plasma biological samples with high sensitivity and specificity. These studies established the physicochemical factors that are important in the design of DAGO: a double-stranded aptamer structure, the presence of two anchoring moieties in the dsDA-Aptamers, and dsDA-Aptamer length.

The double-stranded structure of dsDA-Aptamers was determined to be critical for fluorescence-based target detection by DAGO. Since the nucleobases of dsDNA are shielded within the negatively charged phosphate backbone, the occurrence of π-π stacking interactions between graphene and nucleobases decreases dramatically [20]. A rigid duplex dsDA-Aptamer therefore cannot be adsorbed onto the rGO surface, resulting in the maintenance of strong fluorescence intensity (Fig. II-1B).

For anchoring of dsDA-Aptamers onto rGO nanosheets, the presence of two BHQ1 anchoring moieties, one each in the aptamer and the complementary oligomer, was found to be essential. Only the dsDA-Aptamer containing two BHQ1 moieties showed significant fluorescence intensity; dsAptamers with no or one BHQ1 moiety showed no significant fluorescence upon rGO binding (Fig. II-2B). It has been reported that rGO

nanosheets are involved in π-π stacking interactions with molecules that possess aromatic rings [21]. A BHQ1 molecule contains three aromatic rings, which consequently results in strong π-π stacking interactions with rGO. It has been reported that a fluorophore with a chromophore-like structure similar to that of BHQ1 was able to bind to single walled carbon nanotubes by triggering π-π stacking interaction involving its aromatic fluoresce in isothiocyanate domain [22]. Inclusion of two BHQ1 moieties in dsDA-Aptamers was therefore required to enhance binding to rGO surfaces.

We observed a reduction in the fluorescence intensity of DAGO upon addition of a model target protein IFN-γ, demonstrating the utility of DAGO as a probe for detecting the presence of the target protein. Owing to the greater affinity of the ssAptamer for IFN-γ compared to that of the complementary oligomer strand, the target protein binding resulted in the formation of ssAptamer-target protein complex, the dissociation of dsDA-Aptamers, and fluorescence quenching proportional to the amount of the target protein in the samples. Indeed, surface plasmon resonance studies have demonstrated that target protein binding to an aptamer displaces dsDNA into ssDNA [10]. Upon formation of an ssAptamer-target protein complex, the FAM moiety of the complex comes in close proximity to the rGO surface and thereby enters the effective quenching range of rGO, leading to a considerable decrease in fluorescence intensity.

Sensitivity over a wide dynamic range is an important characteristic of a biosensor. DAGO showed a five-orders-of-magnitude linear dynamic range,

with a limit of detection of 0.1 ng/ml (Fig. II-4). A previous study reported that a gold substrate-anchored electrochemical aptamer biosensor recognized the target protein over a range of 1 - 160 ng/ml [23]. The higher sensitivity of DAGO compared to the aptamer-based electrochemical biosensor might be attributable to the fluorophore-based fluorometric detection principle of dsDA-Aptamers. Previously, a graphene-based sensor was designed for the detection of thrombin [24]. In this latter study, the graphene based sensor showed a linear response over a concentration range of two orders of magnitude. The wide dynamic range of DAGO is like due, in part, to the strong quenching effect of rGO, which broadens the intensity difference compared to the unquenched intensity. A recent study reported that rGO is a better quencher for adsorbed fluorophores than GO and graphite, and exhibits a high quenching efficiency for various fluorophores ranging from green-, red-, and far-red-emitting dyes to quantum dots [25, 26].

In addition to sensitivity, specificity is a crucial component of a biosensor. We found that DAGO showed specificity for the target model protein, IFN-γ, as evidenced by the absence of a fluorescence change in the presence of TNF-a or IL-2 (Fig. II-5). This specificity of DAGO is conferred by the IFN-γ specific aptamer sequence used in the dsDA-Aptamer. The nucleic acid sequence of the IFN-γ specific aptamer has been previously reported [27]. In addition, modifications to aptamer sequences, such as extra DNA

sequences, biotin, or polyethylene glycol, have been reported to have no effect on the affinity between IFN-γ and aptamer [10, 23]. These previous findings are consistent with our observation that the modified ssAptamer sequences used in DAGO retained their affinity for the target protein.

Using DAGO, we were able to quantify the levels of target protein in serum from patients (Fig. II-6). It has been reported that the levels of various cytokines are elevated in the blood of HIV infected patients [16,17]. HIV-patient serum sample was thus chosen to test the feasibility of DAGO for clinical application. Our results demonstrate that DAGO has sufficient specificity and sensitivity for use on clinical samples. The specific detection of target protein using DAGO provides a basis for concluding that a rGO-based fluorescent aptamer-based nano detectors could not only be applied to monitor or diagnose infectious diseases, such as tuberculosis and HIV, but also be used in biochemical studies to analyze cellular secretion of specific cytokines. Although in this study we used IFN-γ as a target model protein in human patient samples, the DAGO concept could be broadly applied to detect other chemicals and cytokines by replacing the aptamer sequences with other target-specific aptamers. Moreover, as shown in Fig. II-6B, the levels of IFN-γ in HIV-positive patient serums revealed good correlation between the proposed assay and ELISA, thereby confirming possibility of practical utilization of the proposed assay.

From an industrial perspective, DAGO has advantages in terms of

processing time and costs compared to conventional cytokine assay systems. Unlike immunoassays which required at least a few hours to complete, the detection of target protein in human patient samples using DAGO required only three steps and took less than 10 min to complete, including 3 min for incubation with human serum samples, 2 min for centrifugation, and 1 min for fluorometric detection. Because DAGO is composed of rGO, a FAM- and BHQ1- labeled DNA aptamer sequence and complementary oligomer, the cost is expected to be lower than that of antibody-based assay systems. Moreover, the higher stability of rGO and DNA compared to antibodies may provide a longer storage time for DAGO.

5. References

[1] Rotem D, Jayasinghe L, Salichou M, Bayley H. Protein detection by nanopores equipped with aptamers. J. Am. Chem. Soc. 2012;134:2781-2787.

[2] Lu CH, Wang F, Willner I. Zn2þ-ligation DNAzyme-driven enzymatic and nonenzymatic cascades for the amplified detection of DNA. J Am Chem Soc 2012;134:10651-10658.

[3] Freeman R, Liu X, Willner I. Chemiluminescent and chemiluminescence resonance energy transfer (CRET) detection of DNA, metal ions, and aptamersubstrate complexes using Hemin/G-Quadruplexes and CdSe/ZnS quantum dots. J. Am. Chem. Soc .2011;133:11597-11604.

[4] Huang Y, Zhao S, Chen ZF, Shi M, Liang H. Amplified fluorescence polarization aptasensors based on structure-switching-triggered nanoparticles enhancement for bioassays. Chem. Commun. 2012;48:7480-7482.

[5] Pelossof G, Tel-Vered R, Willner I. Amplified surface plasmon resonance andelectrochemical detection of Pb2þ ions using the Pb2þ-dependent DNAzymeand hemin/G-quadruplex as a label. Anal. Chem. 2012;84:3703-3709.

[6] Balamurugan S, Obubuafo A, Soper SA, Spivak DA. Surface

immobilization methods for aptamer diagnostic applications. Anal. Bioanal. Chem. 2008;390:1009-1021.

[7] Kirby R, Cho EJ, Gehrke B, Bayer T, Park YS, Neikirk DP, et al. Aptamer-based sensor arrays for the detection and quantitation of proteins. Anal. Chem. 2004;76:4066-4075.

[8] Babendure JR, Adams SR, Tsien RY. Aptamers switch on fluorescence of triphenylmethane dyes. J. Am. Chem. Soc. 2003;125:14716-14717.

[9] Nutiu R, Li Y. Aptamers with fluorescence-signaling properties. Methods. 2005;37:16-25.

[10] Tuleuova N, Jones CN, Yan J, Ramanculov E, Yokobayashi Y, Revzin A. Development of an aptamer beacon for detection of interferon-gamma. Anal. Chem. 2010;82:185-1857.

[11] Rao CN, Sood AK, Subrahmanyam KS, Govindaraj A. Graphene: the new twodimensional nanomaterial. Angew. Chem. Int. Ed. 2009;48:7752-7777.

[12] Miao W, Shim G, Lee S, Choe YS, Oh YK. Safety and tumor tissue accumulation of pegylated graphene oxide nanosheets for co-delivery of anticancer drug and photosensitizer. Biomaterials. 2013;34:3402-3410.

[13] Zhao H, Gao S, Liu M, Chang Y, Fan X, Quan X. Fluorescent assay for oxytetracycline based on a long-chain aptamer assembled onto reduced graphene oxide. Microchim. Acta. 2013;180:829-835.

[14] Kim J, Cote LJ, Kim F, Huang J. Visualizing graphene based sheets by

fluorescence quenching microscopy. J. Am. Chem. Soc. 2010;132:260-267.

[15] Prussin C, Metcalfe DD. Detection of intracytoplasmic cytokine using flow cytometry and directly conjugated anti-cytokine antibodies. J Immunol. Methods. 1995;188:117-128.

[16] Pantaleo G, Koup RA. Correlates of immune protection in HIV-1 infection: what we know, what we don't know, what we should know. Nat. Med. 2004;10:806-810.

[17] Romagnani S. TH1 and TH2 in human diseases. Clin Immunol Immunopathol. 1996;80:225-235.

[18] Karlsson AC, Martin JN, Younger SR, Barry M, Bredt BM, Epling L, et al. Comparison of the ELISPOT and cytokine flow cytometry assays for the enumeration of antigen-specific T cells. J. Immunol. Methods. 2003;283:141-153.

[19] Li M, Zhou X, Guo S, Wu SN. Detection of lead (II) with a ''turn-on'' fluorescentbiosensor based on energy transfer from CdSe/ZnS quantum dots to grapheme oxide. Biosens. Bioelectron. 2013;43:69-74.

[20] Varghese N, Mogera U, Govindaraj A, Das A, Maiti PK, Sood AK, et al. Binding of DNA nucleobases and nucleosides with graphene. Chem. Phys. Chem. 2009;10:206-210.

[21] Bjork J, Hanke F, Palma CA, Samori P, Cecchini M, Persson M. Adsorption of aromatic and anti-aromatic systems on graphene through p-p stacking. J. Phys. Chem. Lett. 2010;1:3407-3412.

[22] Chen H, Wang J, Liang G, Zhang P, Kong J. A novel exonuclease III aided amplification method for sensitive nucleic acid detection based on single walled carbon nanotube induced quenching. Chem. Commun. 2012;48: 269-271.

[23] Liu Y, Tuleouva N, Ramanculov E, Revzin A. Aptamer-based electrochemical biosensor for interferon gamma detection. Anal. Chem. 2010;82:8131-8136.

[24] Chang H, Tang L, Wang Y, Jiang J, Li J. Graphene fluorescence resonance energy transfer aptasensor for the thrombin detection. Anal. Chem. 2010;82:2341-2346.

[25] He S, Song B, Li D, Zhu C, Qi W, Wen Y, et al. A graphene nanoprobe for rapid, sensitive, and multicolor fluorescent DNA analysis. Adv. Funct. Mater. 2010;20:453-459.

[26] Dong H, Gao W, Yan F, Ji H, Ju H. Fluorescence resonance energy transfer between quantum dots and graphene oxide for sensing biomolecules. Anal. Chem. 2010;82:5511-5517.

[27] Lee PP, Ramanathan M, Hunt CA, Garovoy MR. An oligonucleotide blocks interferon-gamma signal transduction. Transplantation. 1996;62:1297-1301

Chapter III

Fucntionalization of nano-graphenes by chimeric peptide engieering

1. Introduction

Since a first exfoliation from graphite, graphene-based nanosheets have received particular attention due to its extraordinary properties including unique structure and mechanical, thermal, optical characteristics [1]. By the courtesy of its planar hydrophobic surface, a graphene nanosheet is a double edged sword in high adsorbing capacity and intense instability in biological condition [2,3]. Increasing application of graphene as a nanomedicine has prompted the researchers to get involved, as many of them are trying to achieve surface functionalization of graphene nanosheets which has been a major concern in biomedical field to improve the therapeutic properties of graphene nanosheets [4, 5].

Non-covalent modification of graphene nanosheets is one of promising strategy which did not alter the intrinsic properties of graphene as compared with covalent conjugation [6]. Peptides are highly favorable molecules for non-covalent functionalization of graphene surface due to its physicochemical diversity and ease of uniform synthesis chemistry [7]. Immobilization of peptide on graphene nanosheets has been diversely elucidated to enable rational functionalization of graphene [8. 9]. In case of targeting ligand, however, direct adsorption on graphene may cause lower binding affinity to target molecules. For this reason, some of peptide ligands were modified on graphene nanosheets after conjugation with anchoring

molecule and PEG spacer [10, 11] which contains complicated synthesis steps.

Buforin IIb (Bu) is synthetic analogue of buforin II originated from a part of histone subunit H2A and notable antimicrobial peptide in its unique mechanism [12]. Unlike other antimicrobial peptides, Bu enters cancer cells without disruption of cell membrane and this feature can be utilized to deliver cargo into cells without non-specific cytotoxicity [13, 14]. As a cellular uptake enhancer, the potential of Bu peptide was previously demonstrated to construct chimeric peptide with scFV [15] and interferon-α [16].

In this study, we designed Bu-derived peptides joined with spacer and anchoring peptide domain for reduced graphene oxide (rGO) nanosheets and examined their secondary structures and cell-penetrating abilities as compared with unmodified Bu peptide. Moreover, these Bu-derived peptides tethered rGO nanosheets were investigated whether the introduction of tethering moiety and repulsive spacer on rGO can maximize activity of peptide ligand with improved cellular internalization and antitumor effect of subsequent photothermal activity of rGO nanosheets.

2. Materials and methods

2.1. Peptides

Four types of peptides were used in this study. The sequence for buforin-derived peptide was RAGLQFPVGRLLRRLLRRLLR (Bu). Bu was modified with seven phenylalanine residues, FFFFFFF-RAGLQFPVGRLLRRLLRRLLR (7F-Bu). To test the role of spacers, four glycine residues or aspartic acid residues were placed between seven phenylalanine residue and Bu sequences; FFFFFFF-GGGG-RAGLQFPVGRLLRRLLRRLLR (7F4G-Bu), and FFFFFFF-DDDD-RAGLQFPVGRLLRRLLRRLLR (7F4D-Bu). All peptides used in this study were purchased from Peptron (Daejeon, Republic of Korea). Secondary structures of peptides were predicted by using a PEP-FOLD server (http://bioserv.rpbs.univ-paris-diderot.fr/services/PEP-FOLD) [17, 18, 19]. For fluorescence labeling of each peptide, 20 μmol of fluorescein 5(6)-isothiocyanate (FITC, Sigma-Aldrich, St. Louis, MO, USA) in 3 mL of anhydrous N,N-dimethylformamide (DMF, Sigma-Aldrich, St. Louis, MO, USA) was added dropwise to a stirred solution of 20 μmol of each peptide and 40 μmol of N,N-diisopropylethylamine (DIPEA, Sigma-Aldrich, St. Louis, MO, USA) in 2 mL of anhydrous dimethyl sulfoxide (DMSO, Sigma-Aldrich, St. Louis, MO, USA). The reaction mixture was stirred for 24 h at room temperature. The mixture was dialyzed against deionized water for 48 h. The resulting FITC-labeled peptides were lyophilized, and stored

at 4°C.

2.2. Preparation of rGO nanosheets

rGO nanosheets were prepared by reducing GO nanosheets. GO nanosheets were prepared from graphite using Hummer's method with slight modification [20]. Briefly, cold H_2SO_4 (23 ml) was added with graphite powder (0.5 g, Sigma-Aldrich), $KMnO_4$ (3 g, Sigma-Aldrich) and NaNO3 (0.5 g, Sigma-Aldrich), and stirred on ice. The resulting mixture was further stirred at 35°C for 1 h. After addition of 46 ml of TDW, the mixture was stirred at 90°C for 1 h. The reaction was stopped with 140 ml of TDW and 10 ml of 30% H_2O_2. The reaction products were washed by repeated centrifugation, first with an aqueous 5% HCl solution, and then with TDW. Finally, the products were dispersed in TDW, sonicated, and centrifuged at 1600 x g for 10 min. The supernatant containing GO nanosheets was collected and an extruder (Northern Lipid, British Columbia, Canada) was used to filter it through 0.2-μm polycarbonate membrane filters (Millipore Corp., Billerica, MA, USA).

The resulting GO nanosheets were used for synthesis of rGO nanosheets. In brief, 2.0 ml of GO nanosheets (5 mg/ml) in TDW was added with 8.0 ml of TDW, 0.5 ml of ammonia solution (28 w/w% in water, Junsei Chemical, Tokyo, Japan), 5.0 μl of hydrazine monohydrate (64 w/w% in water, Sigma-Aldrich). The resultant mixture was stirred at 80°C for 10 min. After cooling

down to room temperature, the excess hydrazine and ammonia was removed by dialysis (MWCO 100K; Spectrum Laboratories, Inc., Rancho Dominguez, CA, USA) against TDW. The obtained rGO nanosheets were stored at 4 ^{o}C until use.

2.3. Preparation of peptide-tethered rGO

For coating the surfaces of rGO with various buforin-derived peptides, rGO nanosheets in TDW (1 mg/ml) were mixed with the same volume of Bu (50 μM), 7F-Bu (50 μM), 7F4G-Bu (50 μM), or 7F4D-Bu (50 μM). Unloaded peptides were removed by gel filtration through a Sephadex G-25M column (GE Healthcare, Piscataway, NJ, USA), yielding peptide-rGO nanosheets. The extent of peptide loading onto rGO was determined by measuring the decrease of fluorescence intensity of FITC-labeled peptides at 525 nm caused by quenching of rGO-adsorbed fluorophores. The fluorescence intensity was measured using a fluorescence microplate reader (Gemini XS; Molecular Device, Sunnyvale, CA, USA).

2.4. Circular dichroism study (CD)

To determine the secondary structure of Bu-derived peptides, CD spectra were obtained using a Circular Dichroism Detector (Chirascan plus, Applied Photophysics Ltd, Surrey, United Kingdom). The spectra were measured between 190 and 260 nm in the presence of 50% (v/v) trifluoroethanol (Thermo Fisher Scientific Inc., Waltham, MA, USA) in phosphate-buffered

saline (PBS). The content of α-helix in Bu-derived peptides was analyzed by CDNN secondary structure analysis software (Applied Photophysics Ltd).

2.5. Size and zeta potential measurement

The lateral sizes of the peptide-rGO nanosheets were measured using dynamic light scattering. The rGO or peptide-rGO nanosheets were diluted with TDW and placed in an ELS-Z (Photal, Osaka, Japan). The hydrodynamic diameters of the nanosheets were determined by He-Ne laser (10 mW) light scattering, and the zeta potential values of rGO and peptide-rGO nanosheets were determined using an ELS-8000 instrument (Photal, Osaka, Japan). The samples were diluted with TDW and zeta potential values were determined by laser Doppler microelectrophoresis at an angle of 22 °C.

2.6. Cell penetrating ability of Bu-derived peptides

The cell penetrating ability of Bu-derived peptides was tested using a BT-20 breast cancer cell line (American Type Culture Collection, Rockville, MD, USA) by flow cytometry. BT-20 cells were seeded onto 48-well plate at a density of 8×10^4 cells/well in 24-well plates. Next day, the cells were treated with FITC-labelled Bu, 7F-Bu, 7F4G-Bu, or 7F4D-Bu at a concentration of 10 μM peptide. After 15 min incubation at 37°C, the cells were harvested and washed thrice with cold PBS containing 2 % fetal bovine serum. Then the cells were analyzed by a BD FACSCalibur flow

cytometry using Cell Quest Pro software (BD Bioscience, SanJose, CA, USA).

2.7. Cellular uptake test of peptide-rGO nanosheets

The cellular uptake of rGO with or without various peptides was tested in BT-20 cells using confocal microscopy and flow cytometry. To visualize the cellar uptake, rGO was labeled with 1,2-distearoyl-sn-glycero-3-phosphoethanolamine- N-[poly(ethyleneglycol) 5000- Alexa Fluor®680 (DSPE-PEG_{5000}-Alexa Fluor®680), as described previously [20] BT-20 cells were seeded onto cover glasses at a density of 8×10^4 cells/well in 24-well plates. Next day, the cells were treated with DSPE-PEG_{5000}- Alexa Fluor®680-labeled plain rGO or peptide-rGO nanosheets at a concentration of 10 μM of each peptide and 80 μg/ml of rGO nanosheets. After 15 min incubation, the cells were washed and fixed with 4% paraformaldehyde (Sigma-Aldrich) in PBS for 15 min, and stained with 4’,6-diamidino-2-phenylindole dihydrochloride (Sigma-Aldrich). The fluorescence intensity of cellular Alexa Fluor®680 was observed using a confocal laser-scanning microscope (LSM 5 Exciter; Carl Zeiss, Inc., Jena, Germany). For flow cytometry, the cells were harvested and washed thrice with cold PBS containing 2 % fetal bovine serum. Then the cells were analyzed by a BD FACSCalibur flow cytometry using Cell Quest Pro software (BD Bioscience).

2.8. Laser irradiation on cells treated with peptide-rGO nanosheets

To test the photothermal effect of peptide-rGO nanosheets upon laser irradiation, the cells were treated with various peptide-rGO nanosheets, and irradiated with near infrared (NIR) laser. BT-20 cells were seeded onto 12-well plates at a density of 1×10^5 cell/well. The following day, cells were treated with plain rGO or peptide-rGO nanosheets at a concentration of 10 μM of peptide and 80 μg/ml of nanosheets. After 15 min incubation, the cells were washed twice with cold PBS and re-suspended in complete RPMI-1640 media. The cell suspensions were irradiated with an 808 nm continuous-wave NIR diode laser (BWT Beijing LTD, Beijing, China) with an output power of 1.2 W. The temperature and thermal images of the graphene-based suspensions during laser irradiation were recorded using an infrared thermal imaging system every 60 seconds (FLIR T420, FLIR Systems Inc, Danderyd, Sweden). Immediately after irradiation, the cells were diluted 5-fold using complete RPMI-1640 media and transferred to 96-well plates for the cell viability assays.

2.9. Quantitative cell viability assay following laser irradiation

The viability of the cells treated with peptide-rGO and laser irradiation was quantified using a fluorescent live cell staining (Invitrogen Corp., Carlsbad, CA, USA) and Cell Counting Kit-8TM (CCK8, Dojindo Molecular Technologies, Inc., Rockville, MD, USA). Briefly, the culture medium was removed, the cells were washed twice with PBS, and 200 μl of

calcein solution (2 μM) was added to each well. After 30 min, the cells were washed twice with PBS and observed under a fluorescence microscope (Leica DM IL; Leica, Wetzla, Germany). For CCK8 assay, 20 μl of CCK-8 (water-soluble tetrazolium salt) solution was added to each well for 30 min, and absorbance was measured at 450 nm using a microplate reader (Sunrise-Basic TECAN, Männedorf, Switzerland). The cell viability in each group was expressed as a percentage of that in control cells.

2.10. Statistics

ANOVA was used for statistical evaluation of experimental data, using Student-Newman-Keuls test for a post-hoc test. All statistical analyses were done using the SigmaStat software (version 3.5, Systat Software, Richmond, CA, USA), and a p-value < 0.05 was considered significant

3. Results

3.1. Biophysical characterization and cell-penetrating ability of buforin-derived peptides

Regardless of spacer amino acids, the modification of Bu peptide with seven phenylalanine residues did not affect the secondary structure and cell-penetrating ability of Bu peptide. Secondary structure prediction results and CD spectra showed the structural similarity of buforin motif between Bu peptide and other three peptides (Fig. III-1). The Bu peptide contains α-helical structure at carboxyl-terminal sequence (Fig. III-1A) which displaying two peaks at 208 and 222 nm in CD spectrum (Fig. III-1E). Similar to Bu peptide, 7F-Bu (Fig. III-1F), 7F4G-Bu (Fig. III-1G), and 7F4D-Bu (Fig. III-1H) showed the characteristic α-helix structures in 50% of trifluoroethanol, which is known to be lipid membrane-mimicking condition [21] in CD spectra. In addition, the sequence modification of Bu peptide in this study did not affect the cell penetration ability. The fluorescence intensity values of cells treated with fluorescent Bu peptides (Fig. III-1I,1M), did not significantly differ those of cell treated with fluorescent 7F-Bu (Fig. III-1J, 1M), 7F4G-Bu (Fig. III- 1K, 1M), and 7F4D-Bu (Fig. III-1L, 1M).

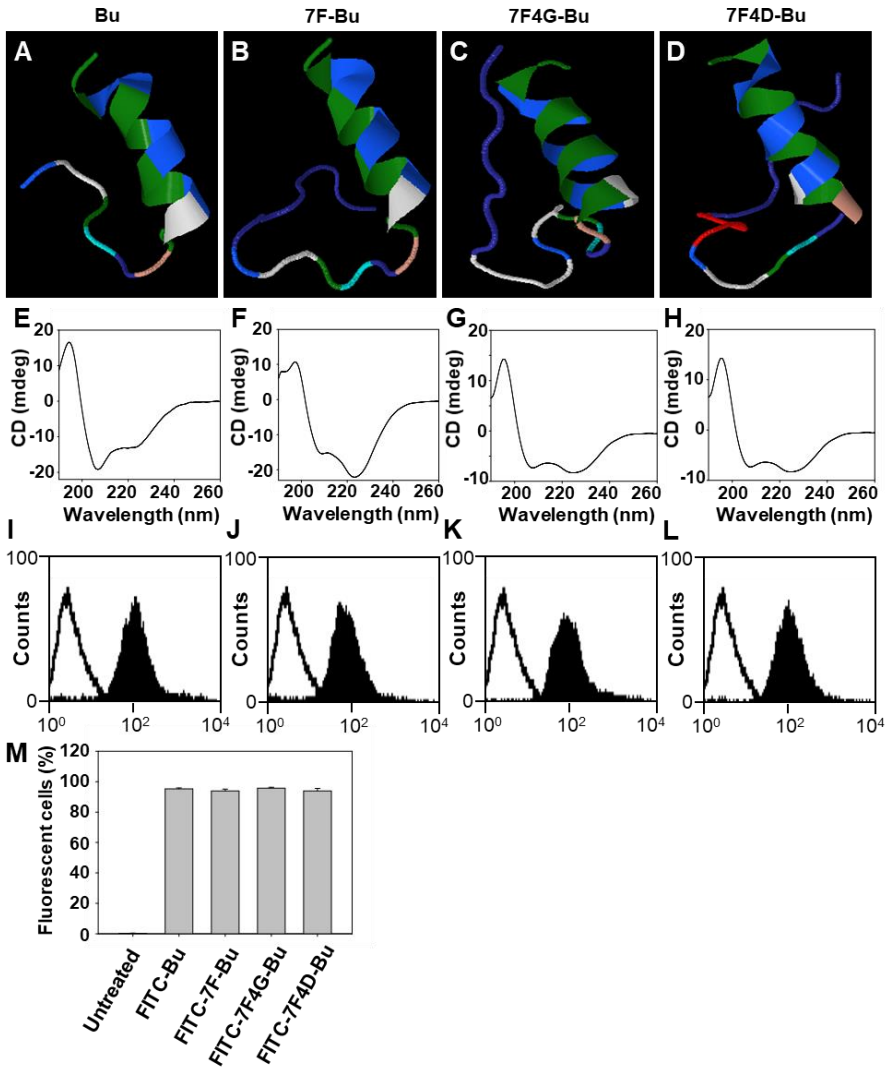

Fig. III-1. Secondary structures of the Bu-derived peptides

Three-dimensional structures of Bu (A), 7F-Bu (B), 7F4G-Bu (C), and 7F4D-Bu (D) were predicted in silico. Each color represents a different amino acid residue. Circular dichroism (CD) spectra of Bu (E), 7F-Bu (F), 7F4G-Bu (G), and 7F4D-Bu (H) were measured in a 1:1 mixture of PBS : TFE (v/v). Cell penetrating efficiency of Bu (I), 7F-Bu (J), 7F4G-Bu (K), and 7F4D-Bu (L) were quantified and fluorescence-positive populations of cells were analyzed by flow cytometry (M).

3.2. Characterization of buforin-derived peptide-rGO nanosheets

The adsorption of buforin-derived peptides on rGO nanosheet did not affect the sizes, but zeta potentials. The predicted adsorption of various buforin-derived peptides on rGO nanosheets (Fig. III-2A) is depicted in Fig. III-2B-2E. Lateral size of plain rGO remained unaffected by surface tethering with buforin-derived peptides (Fig. III-2F). In contrast, surface charge of peptide-tethered rGO nanosheets depended on the type of peptides (Fig. III-2G). Unlike negatively charged plain rGO, the adsorption of Bu increased the zeta potentials to positive values (Fig. III-2H). Among various peptide-tethered rGO nanosheets, 7F4D-Bu-rGO showed the lowest zeta potential values.

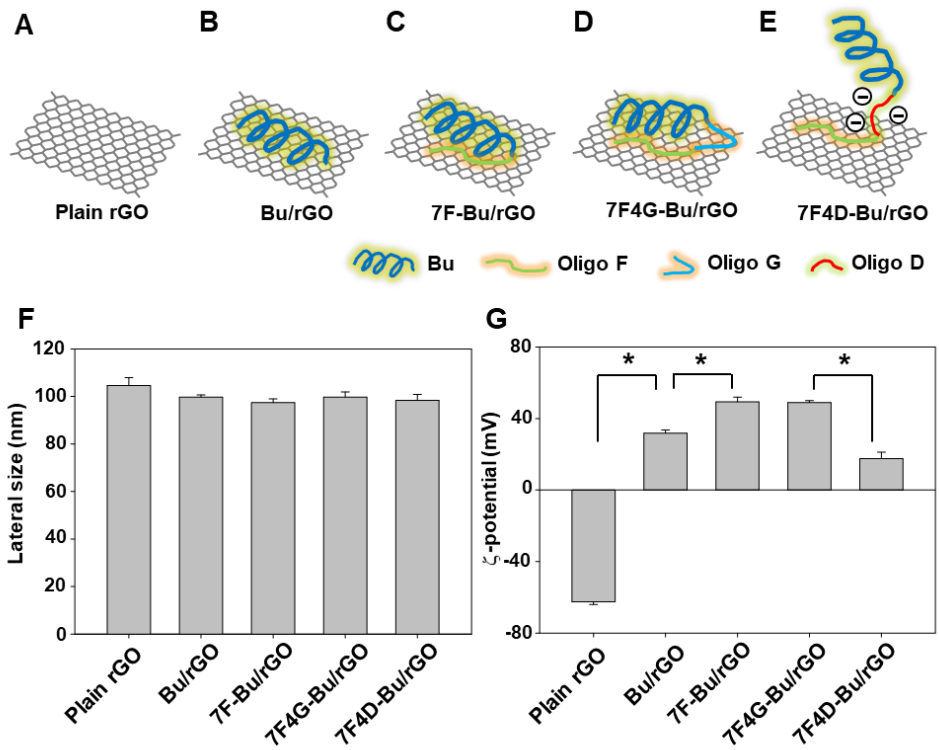

Fig. III-2. Diagrams and characterization of the peptide-tethered rGO

The schematic illustration of plain rGO (A), Bu/rGO (B), 7F-Bu/rGO(C), 7F4G-Bu/rGO (D), and 7F4D-Bu/rGO (E) were described. The lateral sizes of peptide-tethered rGO were measured by dynamic light scattering (F). The zeta potentials were determined using an electro-Doppler method (G). *Significantly different ($p < 0.05$) from each other (ANOVA and Student-Newman-Keuls test).

3.3. Cellular uptake of peptide-tethered graphene nanosheets

Surface coating of rGO with buforin-derived peptides enhanced the cellular delivery of Alexa Fluor®680 lipid-loaded rGO nanosheets. Alexa Fluor®680 lipid-loaded rGO was used to visualize the cellular uptake of rGO nanosheets. For the cellular uptake study, rGO was loaded with Alexa Fluor®680 lipid and each type of peptide. As compared to untreated cells, the cells treated with plain rGO showed negligible increase in fluorescence of Alexa Fluor®680 lipid on rGO nanosheets (Fig. III-3B, 3G). The increase of cellular delivery of rGO was in the order of 7F4D-Bu/rGO (Fig. III-3F, 3G) followed by 7F4G-Bu/rGO (Fig. III-3E, 3G), 7F-Bu/rGO (Fig. III-3D, 3G), and Bu/rGO (Fig. III-3C, 3G).

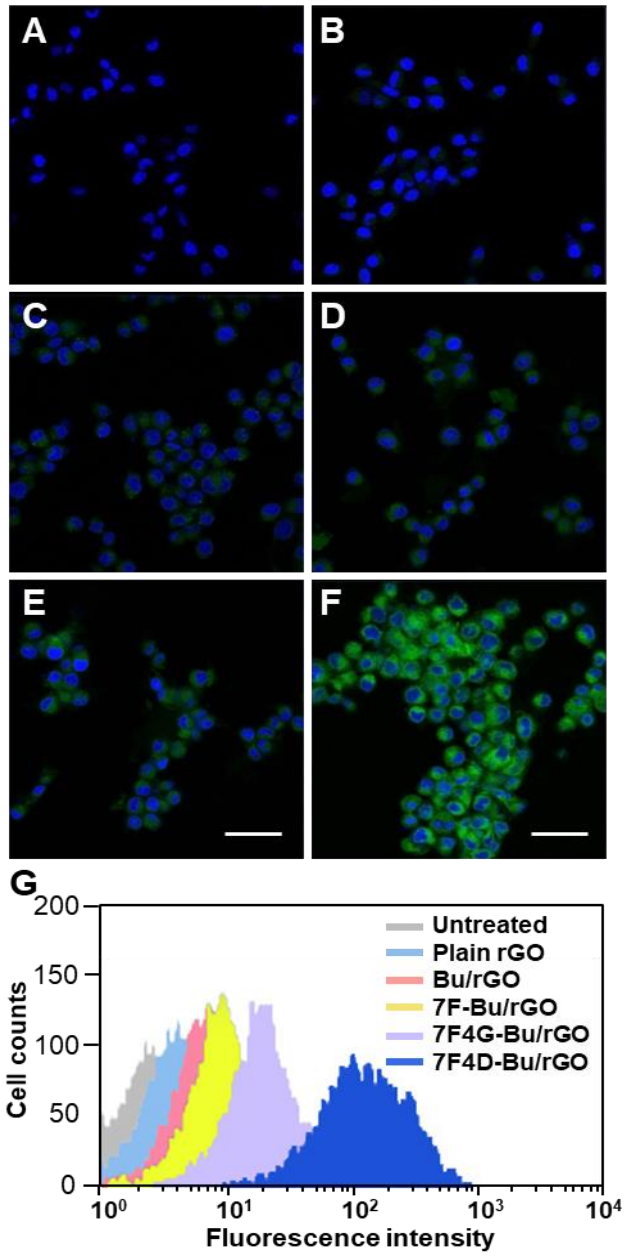

Fig. III-3. Cellular uptake of the peptide-tethered rGO

BT-20 Cells were left untreated (A) or treated with plain (B), Bu (C), 7F-Bu (D), 7F4G-Bu (E), or 7F4D-Bu (F)-tethered rGO. After incubating for 15 min, DSPE-PEG_{5000}-Alexa Fluor 680-modified rGO was observed by confocal microscopy and quantified by flow cytometry (G). Scale bar, 20 μm.

3.4. Photothermal effect of peptide-tethered rGO nanosheets

In line with the cellular uptake of various peptide-tethered rGO, the photothermal effect was affected by the type of buforin-derived peptide on rGO nanosheets. Upon NIR laser irradiation, the cells treated with buforin-derived peptides with space peptide between 7F and Bu showed the higher thermal increase. Between 4D and 4G, the spacer 4D showed the higher thermal increase. 7F4D-Bu/rGO showed the highest temperature increase (Fig. III-4A, 4B) up to 58.3 ± 2.3^{o}C. In the case of the cells treated with 7F4G-Bu/rGO, the temperature was 42.6 ± 1.0^{o}C. The thermal increase of the cells treated with 7F-Bu/rGO or 7F/rGO was significantly lower, showing less than 40 ^{o}C of temperature upon NIR irradiation.

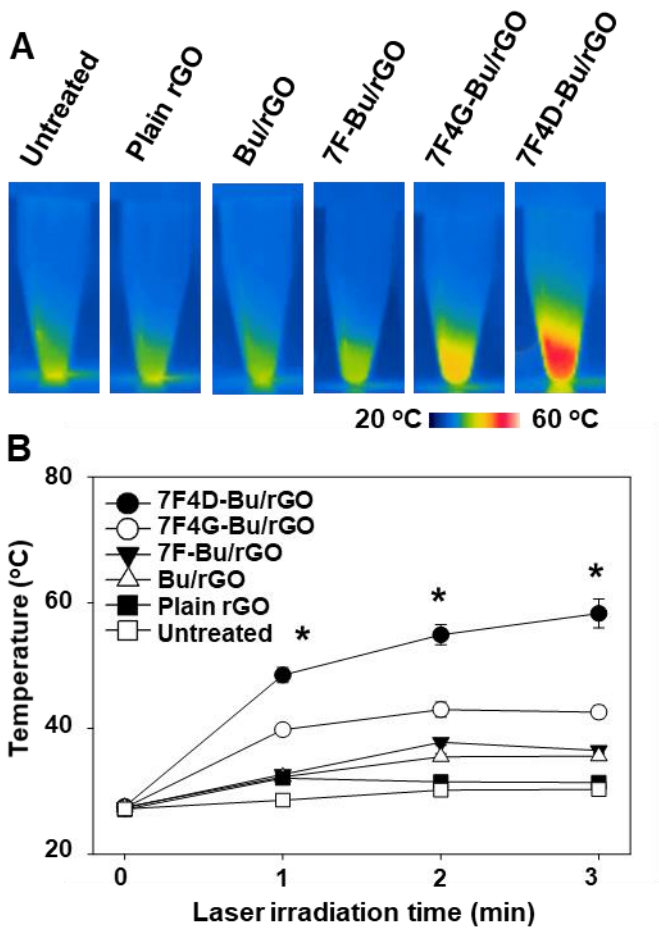

Fig. III-4. Laser-induced photothermal effect of the peptide-tethered rGO

BT-20 Cells were left untreated or treated with plain, Bu, 7F-Bu, 7F4G-Bu, or 7F4D-Bu-tethered rGO for 15 min and then media were replaced with fresh one. After 24 h, the real-time temperature increases upon irradiation of NIR laser from untreated or the rGO-treated cells were observed (A). The highest cell suspension temperature was measured using the FLIR QuickReport 1.2 software (B). *Significantly different ($p < 0.05$) from the other groups at the same time point (ANOVA and Student-Newman-Keuls test).

3.5. Photoresponsive anticancer effect of 7F4D-Bu/rGO nanosheets

The substantial increase of temperature upon NIR irradiation could exert anticancer effects in the cells treated with 7F4D-Bu/rGO nanosheets. The viability of the cells treated with various buforin-derived peptide-tethered rGO was visualized by live cell fluorescence staining with calcein. The live cell staining images showed that the cells treated with 7F4D-Bu/rGO were killed upon NIR irradiation (Fig. III-5F). The quantitation of live cells revealed that the cells treated with 7F4D-Bu/rGO showed the viability of 33.2± 0.4% upon NIR irradiation (Fig. III-5G). Except 7F4D-Bu/rGO, other groups did not show significant decrease of cell viability.

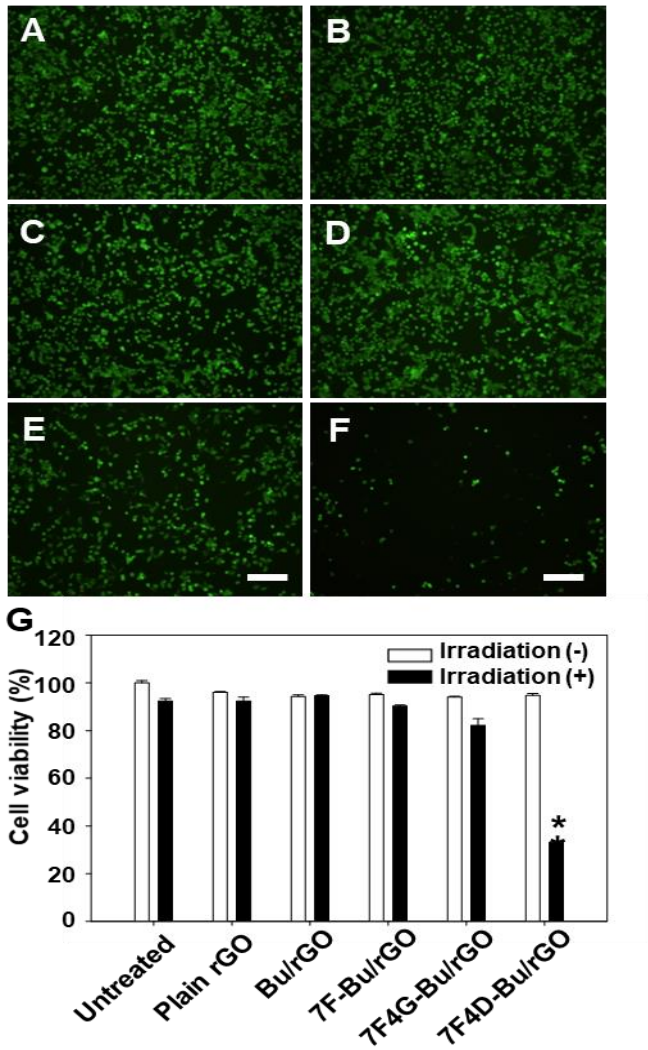

Fig. III-5. Photothermal antitumor effect of the peptide-tethered rGO

BT-20 Cells were left untreated (A) or treated with plain (B), Bu (C), 7F-Bu (D), 7F4G-Bu (E), or 7F4D-Bu (F)-tethered rGO for 15 min and then media were replaced with fresh one. After 24 h, live cells were stained by calcein and observed under a fluorescence microscope (A-F) or the viable cells were measured using the MTT assay after laser irradiation (G). Bar size: 100 μm. *Significantly different ($p < 0.05$) from the other groups (ANOVA and Student-Newman-Keuls test).

4. Discussion

This study demonstrated that engineering of functional peptide, Bu, with anionic four aspartic acids as a spacer and seven phenylalanine residue as an anchoring peptide can lead to the non-covalent tethering of the peptide onto rGO nanosheets, while retaining the biologic activity of the peptide.

In this study, seven phenylalanine-based residue was used as a non-covalent anchoring moiety to rGO nanosheets. Our seven phenylalanine residue has merits in that the simple engineering of peptide sequences can avoid the multi-step covalent modification process for anchoring of functional peptides. Previously, various approaches have been studied to anchor peptides onto graphene-based nanosheets [10, 11, 22, 23] Covalent anchoring of peptide has been reported by coating the surfaces of graphene oxide (GO) with pyrenebutyric acid via π-π interaction, and subsequently conjugating RGD peptide to pyrenebutyric acid (Guo et al. 2012). In another study, interleukin-13 receptor-binding peptide was covalently conjugated to pegylated mesoporous silica-coated graphene nanosheet [10]. Noncovalent anchoring has been mainly done using lipid or peptide moiety. The polyethyleneglycol lipid congjuate of RGD was used to use the hydrophobic lipid moiety as an anchoring moiety to rGO [11]. Recently, nine amino acid-based residue, HNWYHWWPH, was used to attach elastin-like polypeptides of 250 amino acids to graphene nanosheets [23]. However,

there have been limited studies on rGO-binding peptide for anchoring relatively small functional peptide such as buforin, without affecting biological properties.

Driving forces of seven phenylalanine reside adsorption on rGO can be attributed to the hydrophobic interaction between enriched aromatic rings of phenylalanine and planar surface of rGO. Indeed, the parallel orientation of aromatic rings and planar sheet of graphene was reported to contribute to non-covalent π–π interaction of aromatic amino acid phenylalanine with graphene nanosheets [24, 25] reported that aromatic amino acid residues of peptides can maximize the ring-ring off-stack π-π interactions with graphene surfaces.

We observed that the use of four aspartic acid-based (4D) spacer excelled four glycine-based (4G) spacer to retain the biologic activity of rGO-anchored functional peptide (Fig. III-3). Previously, to provide conformational flexibility of functional peptide, oligoglycine has been commonly used as a spacer between anchoring and active peptide domains [7, 25, 26]. Our observation on the enhanced biological property of 7F4D-Bu could be due to the negative surface charges of rGO with carboxyl groups at edge of nanosheets [27]. Charge repulsion between anionic 4D spacer and negatively charged rGO could contribute to the outward orientation of tethered functional Bu for exerting its biological function.

Although we used 7F4D motif for tethering of Bu on rGO, this motif can be further applied for delivery of other functional peptides, and for peptide-

based biosensors for detection and diagnosis. Since peptide-modified rGO nanosheets can be used for detection of enzymes [28, 29], antibodies [30], and cells [31], 7F4D motif can be used to engineer those diagnostic peptides without cumbersome chemical modification. Moreover, the use of homopeptides of seven residues as an anchoring moiety can contribute to cost-effectiveness of peptide engineering.

In conclusion, we provided evidence that 7F4D motif can be used for anchoring functional peptide Bu on rGO without hampering its biological property. The use of 4D contributed to minimize the undesirable interaction of Bu with rGO, resulting in the substantially enhanced cell penetrating property of Bu, as compared to native Bu, or 4G spacer residues. These results suggest the wide application of 7F4D motif for non-covalent tethering of functional peptide onto rGO for protein delivery as well as broad spectrum of peptide-based biosensors on rGO nanosheets

5. References

[1] Wang Y, Li Z, Wang J, Li J, Lin Y. Graphene and graphene oxide: biofunctionalization and applications in biotechnology. Trends Biotechnol. 2011;29(5):205-212.

[2] Miao W, Shim G, Lee S, Oh YK. Structure-dependent photothermal anticancer effects of carbon-based photoresponsive nanomaterials. Biomaterials. 2014;35(13):4058-4065..

[3] Chen J, Liu H, Zhao C, Qin G, Xi G, Li T, Wang X, Chen T. One-step reduction and PEGylation of graphene oxide for photothermally controlled drug delivery. Biomaterials. 2014;35(18):4986-4995.

[4] Georgakilas V, Otyepka M, Bourlinos AB, Chandra V, Kim N, Kemp KC, Hobza P, Zboril R, Kim KS. Functionalization of graphene: covalent and non-covalent approaches, derivatives and applications. Chem. Rev. 2012;112(11):6156-6214

[5] Chen X, Xia Q, Cao Y, Min Q, Zhang J, Chen Z, et al. Imaging the transient heat generation of individual nanostructures with a mechanoresponsive polymer. Nature Communications 2017;8:1498.

[6] Shim G, Kim JY, Han J, Chung SW, Lee S, Byun Y, Oh Y-K. Reduced graphene oxide nanosheets coated with an anti-angiogenic anticancer low-molecular-weight heparin derivative for delivery of anticancer drugs. J. Control. Release. 2014;189:80-89.

[7] Kim SN, Kuang Z, Slocik JM, Jones SE, Cui Y, Farmer BL,

McAlpine MC, Naik RR. Preferential binding of peptides to graphene edges and planes. J. Am. Chem. Soc. 2011;133(37):14480-14483..

[8] Cui Y, Kim SN, Jones SE, Wissler LL, Naik RR, McAlpine MC. Chemical functionalization of graphene enabled by phage displayed peptides. Nano Lett. 2010;10(11):4559-4565.

[9] Zhang Y, Wu C, Guo S, Zhang J. Interactions of graphene and graphene oxide with proteins and peptides. Nanotechnol. Reviews. 2013;2(1):27-45.

[10] Katoch J, Kim SN, Kuang Z, Farmer BL, Naik RR, Tatulian SA, Ishigami M. Structure of a peptide adsorbed on graphene and graphite. Nano Lett. 2012;12(5):2342-2346.

[11] Wang E, Desai MS, Lee SW. Light-controlled graphene-elastin composite hydrogel actuators. Nano Lett. 2013;13(6):2826-2830.

[12] Robinson JT, Tabakman SM, Liang Y, Wang H, Sanchez Casalongue H, Vinh D, Dai H. Ultrasmall reduced graphene oxide with high near-infrared absorbance for photothermal therapy. J. Am. Chem. Soc. 2011;133(17):6825-6831.

[13] Bustillo ME, Fischer AL, LaBouyer MA, Klaips JA, Webb AC, Elmore DE. Modular analysis of hipposin, a histone-derived antimicrobial peptide consisting of membrane translocating and membrane permeabilizing fragments. Biochim. Biophys. Acta. 2014;1838(9):2228-2233.

[14] Jang SA, Kim H, Lee JY, Shin JR, Kim DJ, Cho JH, Kim SC.

Mechanism of action and specificity of antimicrobial peptides designed based on buforin IIb. Peptides. 2012;34(2):283-289.

[15] Verdurmen WP, Brock R. Biological responses towards cationic peptides and drug carriers. Trends Pharmacol. Sci. 2011;32(2):116-124.

[16] Lim KJ, Sung BH, Shin JR, Lee YW, Yang KS, Kim SC. A cancer specific cell-penetrating peptide, BR2, for the efficient delivery of an scFv into cancer cells. PloS One. 2013;8(6):e66084.

[17] Tang Z, Deng H, Zhang X, Zen Y, Xiao D, Sun W, Zhang Z. Effects of orally administering the antimicrobial peptide buforin II on small intestinal mucosal membrane integrity, the expression of tight junction proteins and protective factors in weaned piglets challenged by enterotoxigenic Escherichia coli. Anim. Feed Sci. Technol. 2013;186(3):177-185.

[18] Thévenet P, Shen Y, Maupetit J, Guyon F, Derreumaux P, Tufféry P. PEP-FOLD: an updated de novo structure prediction server for both linear and disulfide bonded cyclic peptides. Nucleic Acids Res. 2012;40:288-293.

[19] Maupetit J, Derreumaux P, Tuffery P. PEP-FOLD: an online resource for de novo peptide structure prediction. Nucleic Acids Res. 2009:37:498-503.

[20] Maupetit J, Derreumaux P, Tufféry P. A fast method for large-scale De Novo peptide and miniprotein structure prediction. J. Comput.

Chem. 2010;31(4):726-738.

[21] Miao W, Shim G, Kang CM, Lee S, Choe YS, Choi HG, Oh YK. Cholesteryl hyaluronic acid-coated, reduced graphene oxide nanosheets for anti-cancer drug delivery. Biomaterials. 2013;34(37):9638-9647

[22] Hao G, Shi YH, Tang YL, Le GW. The intracellular mechanism of action on Escherichia coli of BF2-A/C, two analogues of the antimicrobial peptide Buforin 2. J. Microbiol. 2013;51(2):200-206.

[23] Guo CX, Ng SR, Khoo SY, Zheng X, Chen P, Li CM. RGD-peptide functionalized graphene biomimetic live-cell sensor for real-time detection of nitric oxide molecules. ACS Nano. 2012;6(8):6944-6951.

[24] Wang J, Zhao Y, Ma F-X, Wang K, Wang F-B, Xia X-H. Synthesis of a hydrophilic poly-l-lysine/graphene hybrid through multiple non-covalent interactions for biosensors. J. Mater. Chem. B. Mater. Biol. Med. 2013;1(10):1406-1413.

[25] Rajesh C, Majumder C, Mizuseki H, Kawazoe Y. A theoretical study on the interaction of aromatic amino acids with graphene and single walled carbon nanotube. J. Chem. Physics. 2009;130(12):124911.

[26] Kim SN, Kuang Z, Slocik JM, Jones SE, Cui Y, Farmer BL, McAlpine MC, Naik RR. Preferential binding of peptides to graphene edges and planes. J. Am. Chem. Soc. 2011;133(37):14480-14483.

[27] Mannoor MS, Tao H, Clayton JD, Sengupta A, Kaplan DL, Naik RR, Verma N, Omenetto FG, McAlpine MC. Graphene-based wireless

bacteria detection on tooth enamel. Nat. Commun. 2012;3:763.

[28] Huang H, Chen P, Zhang X, Lu Y, Zhan W. Edge-to-Edge Assembled Graphene Oxide Aerogels with Outstanding Mechanical Performance and Superhigh Chemical Activity. Small. 2013;9(8):1397-1404.

[29] Bhunia SK, Jana NR. Peptide-functionalized colloidal graphene via interdigited bilayer coating and fluorescence turn-on detection of enzyme. ACS Appl. Mater. Interfaces. 2011;3(9):3335-3341.

[30] Kwak SY, Yang JK, Jeon S-J, Kim HI, Yim J, Kang H, Kyeong S, Lee YS, Kim JH. Luminescent Graphene Oxide with a Peptide-Quencher Complex for Optical Detection of Cell-Secreted Proteases by a Turn-On Response. Adv. Funct. Mater. 2014;24(32):5119-5128.

[31] Wu Y-M, Cen Y, Huang LJ, Yu RQ, Chu X. Upconversion fluorescence resonance energy transfer biosensor for sensitive detection of human immunodeficiency virus antibodies in human serum. Chem. Commun.. 2014;50(36):4759-4762.

[32] Wang Z, Huang P, Bhirde A, Jin A, Ma Y, Niu G, Neamati N, Chen X. A nanoscale graphene oxide-peptide biosensor for real-time specific biomarker detection on the cell surface. Chem. Commun. 2012;48(78):9768-9770.

Chapter IV

Cas9-edited immune checkpoint blockade PD-1 DNA polyaptamer hydrogel or cancer immunotherapy

1. Introduction

Recently, immune checkpoint inhibitor-based anticancer immunotherapy has attracted wide attention. Unlike classical chemotherapy, radiotherapy, and surgery, immune checkpoint inhibitors can exert anticancer therapeutic effects by boosting the activity of immune systems. In the tumor microenvironment, the abnormal upregulation of immune checkpoints can reportedly suppress the antitumor function of immune cells [1]. A few immune checkpoint inhibitors have been approved for clinical use to date, and a series of immune checkpoint inhibitors are currently undergoing clinical trials [2]. In general, immune checkpoint inhibitor-based immunotherapy mainly targets molecules that are expressed on immune cells.

Programmed death receptor (PD-1) is a widely studied target immune checkpoint molecule that is expressed on immune cells. The interaction of PD-1 with programmed death-ligand 1 (PD-L1) on tumor cells has been shown to weaken the function of T cells [3]. PD-1 expression is induced in naïve T cells upon activation of T cell receptors [4]. T cell activation results in interferon - γ secretion, which in turn induces high-level surface expression of PD-L1 on cancer [5] Upon interaction with PD-L1, PD-1 inactivates CD28 signaling to weaken T cell activity [6]. The blockade of PD-1 has been studied for the immunotherapy of various cancers, such as

melanoma, non-small cell lung cancer, and head and neck squamous cell carcinoma [7].

Anti-PD-1 antibodies have been clinically used as PD-1 immune checkpoint inhibitor sand studied for co-administration with various chemotherapies [8, 9]. Pembrolizumab, a humanized PD-1 antibody, has shown positive clinical phase 3 results in metastatic non-small cell lung cancer patients when co-treated with pemetrexed and a platinum-based drug [9]. Despite the clinical outcomes obtained with the anti-PD-1 antibodies, some challenges have limited their application. For example, resistance has been seen in certain patients [10]. Moreover, anti-PD-1 antibodies can be rapidly cleared from tumor tissues, potentially via its binding to Fc receptors expressed on tumor-associated macrophages [11]. Finally, the high cost of manufacturing and quality control pose challenges for the widespread application of immunotherapy using anti-PD-1 antibodies [12, 13].

For immune checkpoint blockade, DNA aptamers may serve as an alternative to antibodies. DNA aptamers are composed of oligonucleotides; they are similar to antibodies in that they can bind to target molecules with specificity, but differ in that aptamers exhibit higher thermal stability [14]. Recently, PD-1-targeting aptamers (herein called PD-1 aptamers) have been reported to inhibit the interaction of PD-1 on T cells and PD-L1 on cancer cells, and enhance the activity of T cells [15]. Despite the potential advantages of immune checkpoint-inhibiting aptamers, however, they do not show strong retention in the body, and thus have not been widely studied.

Researchers have sought to increase the retention of aptamers in the body, such as by using conjugation with polymers (e.g., polyethyleneglycol) to increase the effective size of the formulation [16] or by applying nanocarrier-mediated delivery [17]. Although DNA hydrogels harboring repeating immune checkpoint aptamer sequences could exhibit increase retention, the need to precisely cleave the DNA to generate the proper aptamer sequence has remained a hurdle.

CRISPR-associated protein 9 (Cas9) has been mainly studied in the context of gene editing, such as in therapeutics and agricultural products. It is complexed with a single-strand guide RNA (sgRNA) [18], which binds specific sequences of double-stranded DNA to allow Cas9 to make a precise cut [19, 20]. Cas9/sgRNA has been studied as a means to treat amyotrophic lateral sclerosis and hypercholesterolemia [21, 22]. To date, however, few studies have examined the use of Cas9/sgRNA for the controlled release of DNA aptamers from hydrogels.

In the present study, we utilized the precise double stranded DNA-editing function of Cas9/sgRNA to design a DNA hydrogel that can release PD-1 aptamers in a programmed manner. We formed DNA polyaptamer hydrogels using a rolling-circle amplification (RCA) method. The RCA products, which contained repeats of the aptamer along with sgRNAs encoding target or complementary target sequences, were crosslinked via internal sites to form the hydrogel. Upon exposure to Cas9/sgRNA, the hydrogels released the PD-1 DNA aptamers in a sustained manner at the site of administration,

and exerted antitumor effects by enhancing the activation of immune systems.

2. Materials and methods

2.1. Construction of polymeric PAH

PD-1 DNA aptamer hydrogel (PAH), which can generate PD-1 aptamers by Cas9/sgRNA specific cleavage, was prepared by rolling circle amplification (RCA) of two template sequences, which were subsequently hybridized. The sequences were as follows: RCA template 1, 5'-GAGCGACGGACGGAAGCGGCATACGTGTAGTGCAGGGACGGGAACTGTACCGTCTGTGCCGTCACCGCTATCGTC*CCCTGAAGTTCATCTGCACCACC*-3', where the template for the PD-1 aptamer [15] is underlined and that for the sgRNA target sequence is italicized; and RCA template 2, 5'-*AACTTCAGGG*GAGCGACGGACGGAAGCGGCATACGTGTAGTGCAGGGACGGGAACTGTACCGTCTGTGCCGTCACCGCTATCGTC*GGTGGTGCAGATG*-3', where the template for the PD-1 aptamer is underlined and that for the complementary sgRNA target sequence is italicized. To generate the pre-circular RCA template, 0.5 mM of each DNA template (Macrogen Inc., Daejeon, Republic of Korea) was annealed with 0.5 mM of each template-specific primer (5'-GTCGCTCGGTGGTGCAGATGAA-3' and 5'-TCCCCTGAAGTTCATCTGCACC-3'; Macrogen Inc.) in hybridization buffer (1 mM EDTA, 10 mM Tris HCl, 100 mM NaCl, pH 8.0). The mixture of pre-circular RCA template and primer was reacted with T4 DNA ligase (125 units/mL; Thermo Scientific, Waltham, MA, USA) for 12 h at 4 °C to

close the nick. The T4 DNA ligase was then inactivated by incubation for 5 min at 70 °C. The resulting circular template was subjected to RCA by incubation with phi29 DNA polymerase (100 units/mL; Thermo Scientific) and 2 mM dNTPs (ELPIS-Biotech. Inc., Daejeon, Republic of Korea) for 48 h at 30 °C. The phi29 DNA polymerase was inactivated by incubation for 10 min at 70°C, and the RCA products were separated by centrifugation at 3,000 g for 10 min, and re-suspended in triple distilled water (TDW). Cas9-cleavable PAH was prepared by hybridizing the two RCA products at a 1:1 weight ratio, with a final concentration of 2.5 mg/ml.

2.2. Rheological characterization

The rheological properties of the DNA hydrogel were measured using a rotational rheometer (DHR-1; TA Instruments Ltd., New Castle, DE, USA). PAH (2.5 mg/ml) was incubated with or without Cas9/sgRNA (1 mg/ml) for 4 days at 37°C. On the rheometer, each sample was twisted using dynamic frequency sweeping mode with strain fixed at 5 %. As rheological parameters, storage modulus, loss modulus, and viscosity were measured. The change of viscosity in Cas9/sgRNA- and -untreated samples was also compared by observing their behavior in vials subjected to inversion.

2.3. Scanning electron microscopy (SEM)

The morphologies of PAH with or without Cas9/sgRNA treatment were examined by SEM. For Cas9 treatment, PAH (2.5 mg/ml) was treated with Cas9/sgRNA (1 mg/ml) for 4 days at 37°C. For SEM observation, the

samples were freeze dried (FD8-8602; Operon, Republic of Korea) and spray-coated with Au/Pd (EM ACE200; Leica, Austria). The morphologies of the samples were observed at different magnifications under a field-emission scanning electron microscope (Supra 55VP, Carl Zeiss, Oberkochen, Germany).

2.4. Measurement of swelling ratio

The swelling ratios of PAH and PAH/Cas9 were measured by calculating the water uptake capacity over time. Lyophilized powders of each DNA hydrogel (15.3 mg) were placed in 2 ml of triple-distilled water with or without Cas9/sgRNA, and their weights were measured at various time points. The swelling ratio at each time point was calculated by the equation: swelling ratio (%) = [(W2-W1)/W1] x 100, where W1 is the weight of the dehydrated gel and W2 is the weight of the hydrated gel.

2.5. Measuring the Cas9-mediated cleavage of PAH

To induce Cas9-mediated cleavage, PAH was incubated with Cas9 plus its guiding sgRNA, which was synthesized using a GeneArt precision gRNA synthesis kit (Thermo Scientific) according to the manufacturer's protocol. The sgRNA sequence was: 5'-GGUGGUGCAGAUGAACUUCAGUUUUAGA GCUAGAAAUAGCAAGUUAAAAUAAGGCUAGUCCGUUAUCAACUU GAAAAAGUGGCACCGAGUCGGUGCUUUU-3' (the target sequence is underlined) (29). Cas9 protein (1.8 mg/ml, Cosmogenetech, Daejeon, Republic of Korea) and sgRNA (4 mg/ml) were pre-mixed at a weight ratio

of 2:1 to form Cas9/sgRNA complexes, and this mixture was combined with PAH at various ratios in NEBuffer™ 3.1 (New England BioLabs, Ipswich, MA, USA). The reaction was allowed to proceed at 37 °C for various durations. At the end of each incubation, the mixture was treated with RNase (0.25 mg/ml; Qiagen, Valencia, CA, USA) to eliminate the sgRNA. The reaction mixtures were resolved on a 1% agarose gel and visualized with Safe-Pinky dye (GenDepot, Barker, TX, USA) and a Gel DocTM imaging system (Biorad, Hercules, CA, USA).

2.6. Splenocyte test for the ability of PAH/Cas9 to block PD-1

The Cas9 cleavage-mediated generation of PD-1 aptamers from PAH was tested by monitoring the secretion of interleukin-2 (IL-2) by splenocytes, which was taken as reflecting the interaction between PD-1 and PD-L1. To mimic the in vivo interaction between PD-1 and PD-L1, each 96-well plate was pre-coated with 15 μg/ml PD-L1 and Fc protein (BioLegend, San Diego, CA, USA) in PBS overnight at 4 ºC. Splenocytes isolated from C57BL mice (Raon Bio Korea, Yongin, Republic of Korea; Approval No. SNU-180508-1) were seeded to the plate (2×10^5 cells/well) and cultured in RMPI supplemented with 10% FBS, 1% penicillin/streptomycin, and 2 μg/ml anti-mouse CD28 antibody (BioLegend). The splenocytes were incubated for 48 h with anti-mouse PD-1 antibody (20 μg/ml, BioLegend), free PD-1 DNA aptamer (46 μg/ml), PAH (46 μg/ml) alone, or with the reaction product of PAH (46 μg/ml) plus Cas9/sgRNA complex. In some

experiments, splenocytes were activated by being cultured in wells precoated with 10 μg/ml anti-mouse CD3 antibody (BioLegend) and in complete RPMI supplemented with 2 μg/ml anti-mouse CD28 antibody (BioLegend). The supernatants of activated splenocytes or hydrogel treated splenocytes were collected and the levels of IL-2 were determined using an enzyme linked immunosorbent assay (ELISA) kit (R&D Systems, Minneapolis, MN, USA). The secretion level of IL-2 in each group was normalized with that of the corresponding activated splenocytes.

2.7. Molecular imaging at injection sites

The retention of PAH at the injection sites was measured by molecular imaging of fluorescent dye-loaded hydrogels. For imaging, the free PD-1 DNA aptamer or PAH were labeled with a Cy5.5-tagged complementary probe (5'-TGTAGTGCAGGGACGGGGAACTGTACCGTCTG-3'; Macrogen). Fluorescent probe-labeled free PD-1 DNA aptamer, PAH, or PAH/Cas9 were subcutaneously injected into the hind legs of C57BL/6 mice (Raon Bio Korea Co., Ltd, SNU180508-1). The retention of each sample at the injection site was observed by monitoring the Cy5.5 signal using an IVIS® Spectrum CT (Perkin Elmer, Waltham, MA, USA)

2.8. In vivo test of antitumor effect

The antitumor effect of the Cas9-cleavabled PD-1 DNA aptamer hydrogel was tested in vivo using a B16F10 melanoma model, which was chosen for its high-level expression of PD-L1 [30, 31]. To establish the tumor model,

PD-L1-overexpressing B16F10 melanoma cells (1 x 10^5 cells) were inoculated into the right flanks of C57/BL6 mice (Raon Bio KoreaWhen the tumor volumes reached 20 mm^3 , the mice were intratumorally treated with 50 μg of PD-1 DNA aptamer, PAH, or Cas9/PAH. After the first injection, the mice were treated three more times at 4-day intervals. Tumor sizes were measured using a caliper (Mitutoyo, Aurora, IL, USA), and the tumor volume was calculated according to the equation a x b^2 x 0.5, where a is the largest length and b is the smallest length. Tumor volume was monitored over 20 days after tumor inoculation. The tumor tissue samples were taken 20 days after the tumor inoculation. The expression of PD-L1 on B16F10 melanoma was confirmed by incubating cells with an antimouse PD-L1 antibody (BioLegend) for 1 h followed by Alexafluor 647-tagged goat anti-rat IgG antibody (1:100; BioLegend), and examining the expression of PD-L1 by flow cytometry (BD FACSCalibur; BD Biosciences, Becton Dickinson, NJ, USA).

2.9. Measurement of tumor-infiltrated lymphocytes

At the endpoint of the in vivo antitumor efficacy test (day 20 after inoculation of B16F10 tumor cells), the population of infiltrated lymphocytes in tumor tissues were harvested from each group and tested by flow cytometry. Single-cell suspensions were prepared by incubating tumor tissues with 1 mg/mL of collagenase (Sigma-Aldrich) at 37 ºC for 3 h. The obtained cell suspensions were filtrated through a cell strainer (40-μm pore

size, Cat # 93040; SPL Life Science, Pocheon, Republic of Korea) and the filtrate was centrifuged at 210 xg for 5 min to remove debris [32]. The cell pellets were washed three times with phosphate-buffered saline. The cells were resuspended in PBS and incubated with rat anti-mouse CD 4 (Cat # 100401, BioLegend) or rat anti-mouse CD8a (Cat # 100702, BioLegend) for 1 h followed by Alexafluor 647-tagged goat anti-rat IgG (Cat # 405416, BioLegend) for 1 h. The populations of CD4+ or CD8+ T cells were analyzed by flow cytometry (BD FACSCalibur; BD Biosciences).

2.10. Statistics

Experimental data were analyzed by two-sided analysis of variance (ANOVA) with the Student-Newman-Keuls post-hoc test. All statistical analyses were performed using the SigmaStat software (version 12.0; Systat Software, Richmond, CA, USA). A p-value less than 0.05 was considered statistically significant.

3. Results

3.1. Construction of a Cas9-cleavable PD-1 DNA aptamer hydrogel

The Cas9-cleavable PD-1 DNA polyaptamer hydrogel (PAH) was formed by the hybridization of two RCA products. The composition of each RCA template is illustrated in Figure IV-1A. One could be used to generate long repeats of the PD-1 aptamer and the sgRNA target sequence, while the other could be used to generate long repeats of the PD-1 aptamer and the corresponding sgRNA target-binding sequence. Base pairing between the sgRNA target and target-binding site allowed these RCA products to undergo sequence-specific hybridization (crosslinking), this both formed a gel and, when Cas9 was present, guided the enzyme in providing specific cleavage.

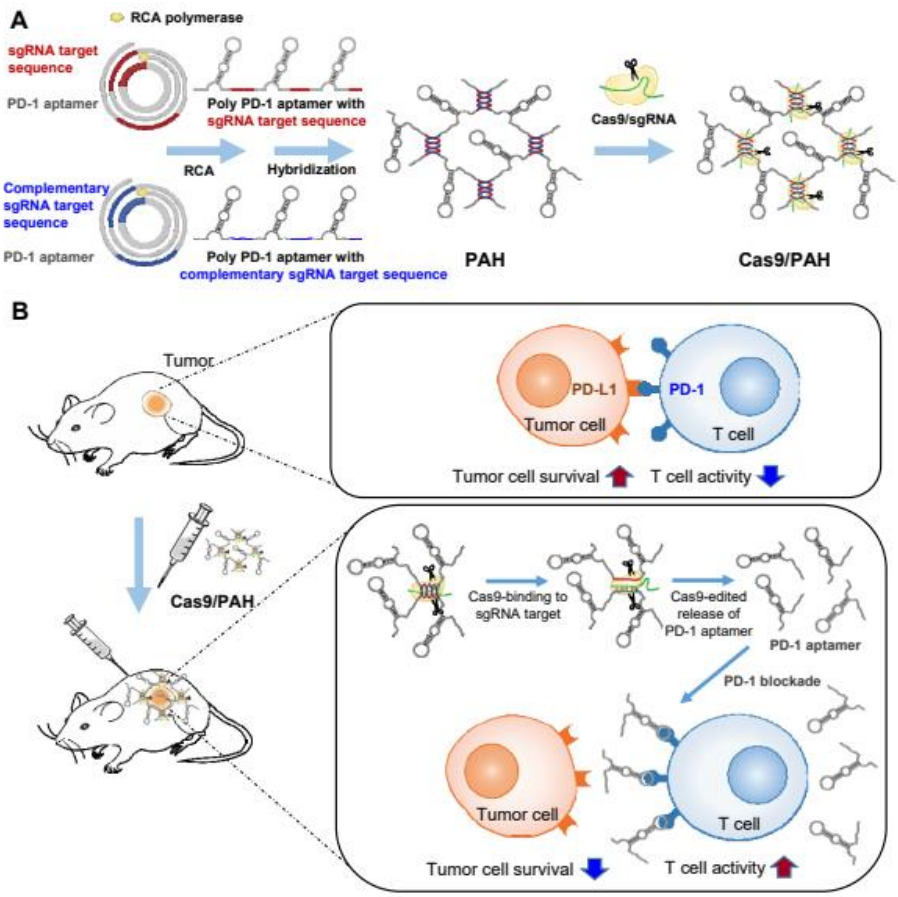

Figure IV-1. Illustration of the Cas9/sgRNA-edited immune checkpoint-blocking DNA polyaptamer hydrogel and its action mechanism

(A) To construct a Cas9/sgRNA-edited immune checkpoint-blocking DNA polyaptamer hydrogel, two types of RCA templates were designed. Both contained the PD-1 DNA aptamer sequence, but they differed in that one contained the sgRNA target sequence for Cas9/sgRNA specific cleavage, while the other contained the complementary sgRNA target sequence. The two RCA products were crosslinked by sequence-specific hybridization between the sgRNA target and complementary sequences. (B) In the tumor microenvironment, the precise excision of the PD-1 aptamer by Cas9/sgRNA can block the interaction between immune cell-surface PD-1 and tumor cell-surface PD-L1, enhancing immune cell activation for immunotherapy.

3.2. Characterization of Cas9-cleavable PD-1 DNA polyaptamer hydrogel

The generated PAH showed altered physicochemical behaviors when treated with Cas9/sgRNA complexes, as assessed by analysis of its rheology, swelling ratio, and morphology. In the absence of Cas9/sgRNA, PAH remained in its original position in a tube that was subjected to inversion (Fig. IV-2A). In contrast, PAH mixed with Cas9/sgRNA (Cas9/PAH) followed the movement of inversion, winding up on the underside of the lid (Fig. IV-2A). In terms of rheological properties, PAH exhibited a higher storage modulus compared to its loss modulus indicating its gel property (Fig. IV-2B), whereas the storage modulus and loss modulus of Cas9/PAH were both close to zero (Fig. IV-2C). In terms of viscosity, that of PAH decreased as the oscillation frequency increased, whereas Cas9/PAH lacked this shear-thinning property due to loss of viscosity (Fig. IV-2D). The swelling behavior of the hydrogel also differed in the absence and presence of Cas9/sgRNA. The lyophilized powder form of PAH could immediately rehydrate to hydrogel, showing a swelling ratio of 757.8 ± 15.9% over 2 h, whereas Cas9/PAH exhibited no such swelling function (Fig. IV-2E). Finally, SEM revealed that the hydrogel had different morphologies in the presence or absence of Cas9/sgRNA: PAH exhibited a porous structure (Fig. IV-2F) while Cas9/PAH failed to show any porosity (Fig. IV-2G).

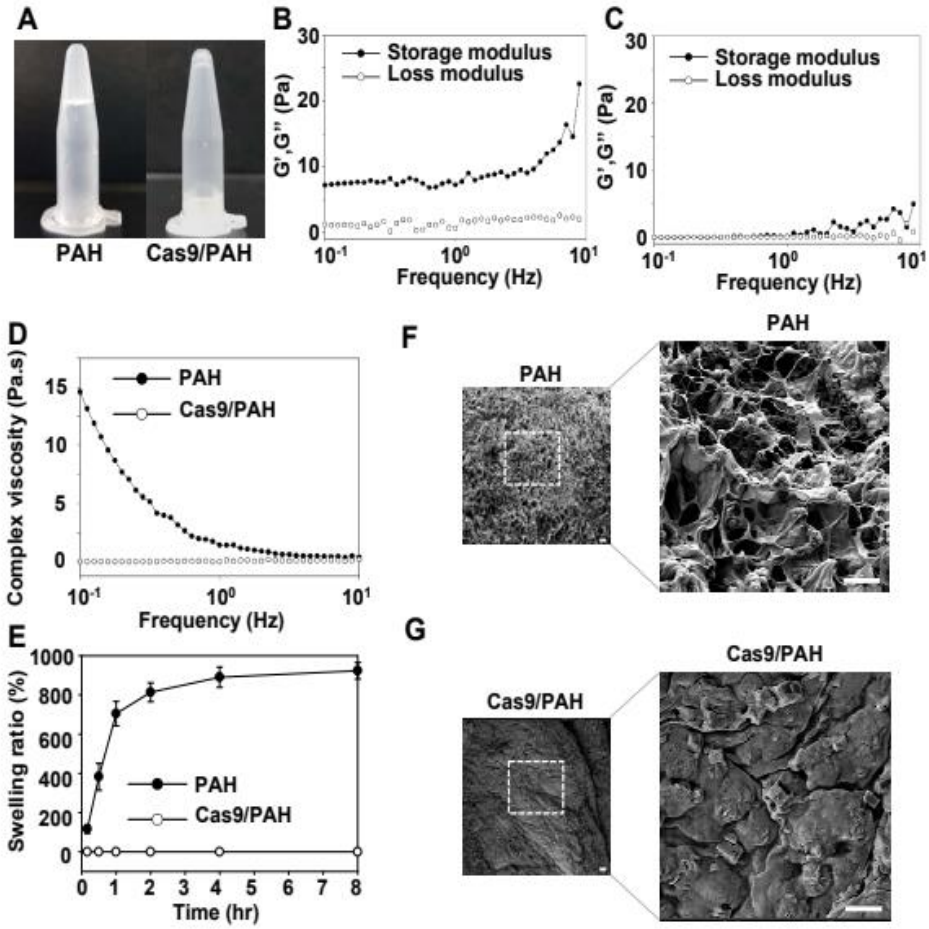

Figure IV-2. Physicochemical properties of the hydrogel

(A) Morphologies of PAH in the absence and presence of Cas9/sgRNA. Photographs show (left) PAH before addition of Cas9/sgRNA, with the container inverted to show the gel property, and (right) Cas9/PAH incubated for 4 days, with the container inverted to show the loss of gelation. (B and C) The storage modulus and loss modulus were measured for PAH (B) and Cas9/PAHincubated for 4 days (C). (D) Viscosity was measured for PAH and Cas9/PAH incubated for 4 days. (E) The swelling rate of Cas9/PAH was tested by soaking the lyophilized powder in triple distilled water. (F and G) SEM images of PAH (F) and Cas9/PAH incubated for 4 days (G) were presented in different magnification ratios. Scale bars indicate 10 μm.

3.3. In vitro Cas9-edited cleavage of PAH

We used an in vitro study to examine the cleavage of PAH by Cas9/sgRNA at different ratios of hydrogel, Cas9, and sgRNA. Electrophoretic experiments revealed that when the weight ratio of PAH, Cas9, and sgRNA was 10:2:1, complete cleavage of the hydrogel (i.e., full liberation of the PD-1 aptamer) was observed within 3 days (Fig. IV-3).

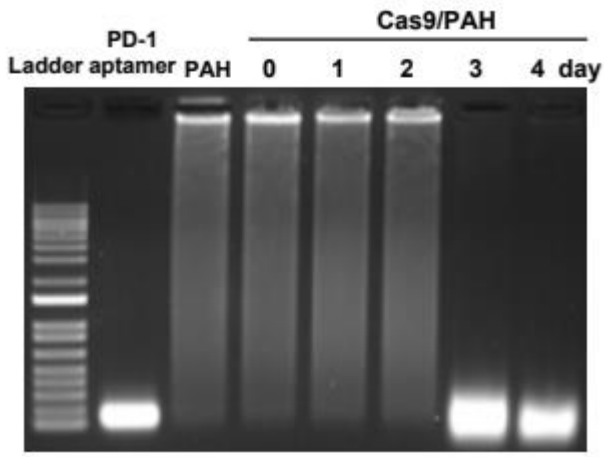

Figure IV-3. Cas9/sgRNA-edited cutting and release of the PD-1 aptamer from PAH

The cutting and release of the PD-1 DNA aptamer from PAH was tested by gel electrophoresis. PD-1 aptamer, PAH alone, or Cas9/PAH (incubated together for the indicated days) were electrophoresed on an agarose gel.

3.4. In vivo degradation of hydrogel at the injection site

PD-1 aptamer solution, PAH, and Cas9/PAH differed in their retention at the subcutaneous injection site of mice. Measurement of retention performed using a Cy5.5-tagged complementary probe revealed that both PAH and Cas9/PAH were retained longer than the free aptamer solution in mice. The group treated with PD-1 aptamer solution showed rapid disappearance of the fluorescence signal within 1 day post-injection. The group treated with PAH showed a prolonged fluorescence signal up to 3 days after administration. Compared to PAH, Cas9/PAH showed faster degradation at the injection site (Fig. IV-4).

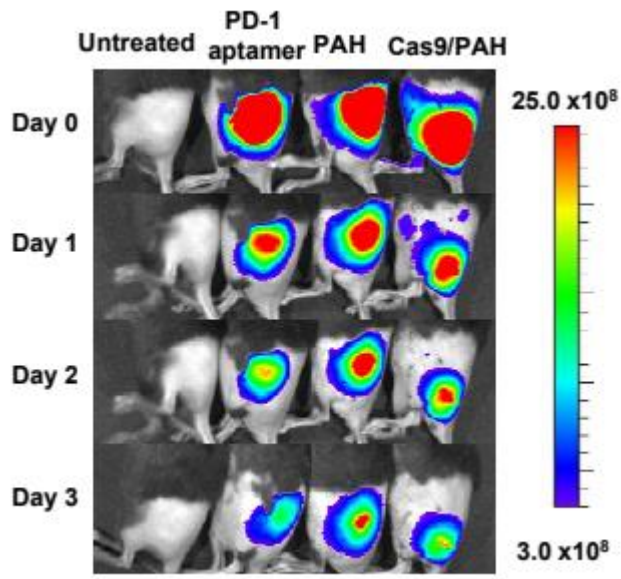

Figure IV-4. Retention of Cas9/PAH at the injection site

Mice were subcutaneously injected with various samples tagged with Cy5.5 fluorescent probe. The retention of each sample at the injection site was observed using an IVIS® Spectrum CT.

3.5. In vitro splenocyte-blocking effect of Cas9/PAH

To examine the Cas9/sgRNA-mediated liberation of PD-1 aptamers from PAH, we monitored the secretion of IL-2 from splenocytes. The in vivo interaction of PD-1 with PD-L1 was mimicked by culturing splenocytes on PD-L1-precoated or un-coated plates. The interaction between PD-1 on the splenocytes and PD-L1 on the plate was expected to suppress the secretion of IL-2 by splenocytes, as illustrated in Figure 5A. The results revealed that the secretion of IL-2 differed among splenocytes treated with PD-1 aptamer, PAH, and Cas9/PAH (Fig. IV-5B). Compared to splenocytes cultured on a plain culture plate, whose IL-2 secretion was designated 100% and used for normalization, those cultured on precoated plates exhibited a sharp reduction in IL-2 secretion (down to 25%). When splenocytes cultured on a PD-L1-coated plate were treated with PD-1 aptamer solution, PAH alone, or Cas9/PAH, their IL-2 secretion was recovered to 52.4 ± 5.4%, 63.3 ± 7.5%, and 85.6 ± 3.0%, respectively. The recovery of IL-2 secretion triggered by Cas9/PAH was significantly higher than that obtained with PAH alone.

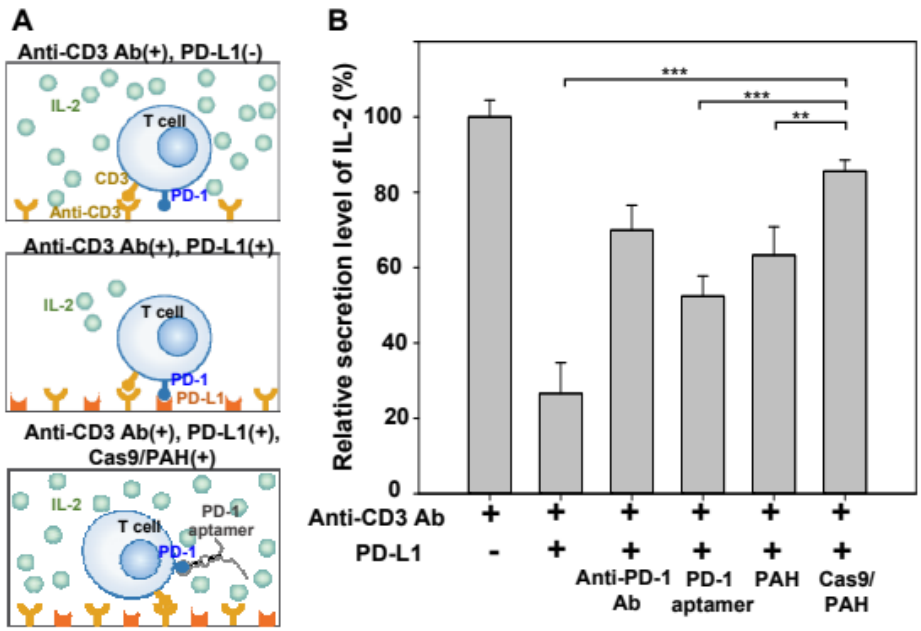

Figure IV-5. In vitro activation of splenocytes by Cas9/PAH

(A) Splenocytes were cultured on PD-L1-precoated plates and exposed to the various treatments, and their IL-2 secretion was measured. (B) The levels of IL-2 secreted by the various treatment groups, as assessed by ELISA (n=4).

3.6. In vivo antitumor effect of PD-1 DNA aptamer hydrogel plus Cas9/sgRNA

The co-treatment of tumor-bearing mice with PD-1 DNA aptamer hydrogel plus Cas9/sgRNA (Cas9/PAH group) showed the highest antitumor effect among the tested interventions. The dosing schedule is depicted in Figure 6A. The groups treated with free PD-1 aptamer or PAH alone did not exhibit any significant between-group difference in tumor volume (Fig. 6B and 6C). Compared to these groups, Cas9/PAH-mice showed a significantly smaller tumor volume (Fig. IV-6D). In the survival study, the free PD-1 aptamer- and PAH-treated groups both had 0% survival, whereas the Cas9/PAH-treated group exhibited 60% survival at day 45 after tumor inoculation (Fig. IV-6E).

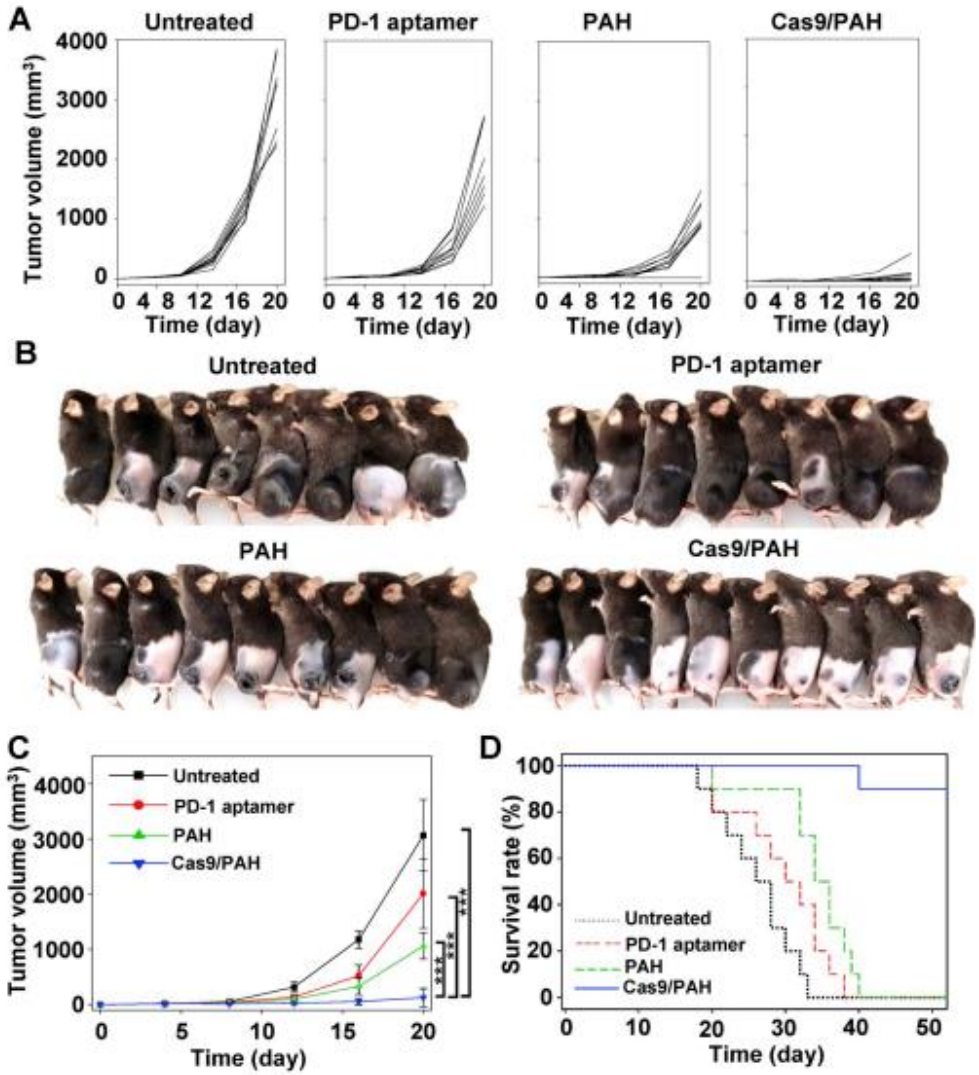

Figure IV-6. In vivo antitumor effect of Cas9/PAH

(A) B16F10 tumor-bearing mice (10 mice per group) were repeatedly treated with the various formulations at 4-day intervals from day 4 after tumor inoculation. The tumor volumes of each mouse were plotted with time. (B) At day 20 after the tumor inoculation, the survived mice in each group were photographed. (C) The mean tumor volume of each group was presented with error bars over time. (D) The survival rates of each group were recorded up to 52 days after tumor inoculation.

3.9. Infiltration of T cells into tumor tissues

To begin examining the mechanism by which Cas9/PAH conferred higher antitumor efficacy, we assessed the infiltration of T cells in the tumor tissues. In the group treated with free PD-1 aptamer, the infiltration of tumor tissues was less than 0.05% for both CD4+ T cells (Fig. IV-7A) and CD8+ T cells (Fig. IV-7B). In the PAH group, the infiltration of T cells was slightly but not significantly increased to 0.09 ± 0.03% for CD4+ T cells and 0.10 ± 0.03% for CD8+ T cells (Fig. IV-7C). Notably, the Cas9/PAH group showed significantly higher infiltration of T cells: that of CD4+ T cells was 4.5 ± 1.0%, which was a 50.1-fold increase compared to the PAH group (Fig. IV-7C); and that of CD8+ T cells was 3.8 ± 0.4%, which was a 38-fold increase relative to the PAH group (Fig. 7D).

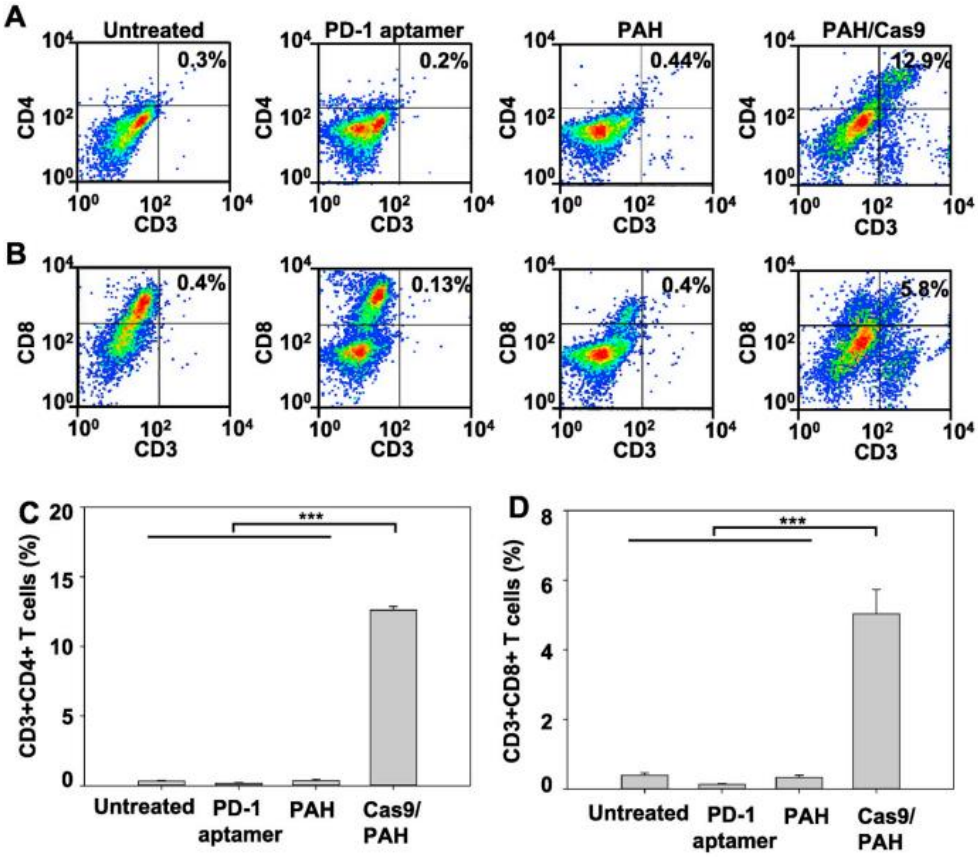

Figure IV-7. Infiltration of T cells to tumor tissues

B16F10 tumors were repeatedly treated with the various formulations from day 4 after tumor inoculation, with 4-day intervals. At day 28 after tumor inoculation (6 doses), tumor tissues were digested and stained with APC tagged rat anti-mouse CD3 antibody and PE tagged rat anti-mouse CD4 antibody and PerCP/cyanine5.5 tagged rat anti-mouse CD8a antibody. The populations of tumor-infiltrating CD3+ CD4+ (A, C) and CD3+CD8+ (B, D) T cells were analyzed by flow cytometry. Representative dot plots of single-cell suspensions subjected to flow cytometry for CD3+ CD4+ T cells (A) and CD3+ CD8+ T cells (B). Percentages of CD3+CD4+ (C) and CD3+CD8+ (D) T cell populations in the tumor tissues (n = 4).

4. Discussion

For DNA polymerized aptamer therapy, the precise editing and release of aptamers is crucial, but not has been accomplished as yet. In this study, we demonstrated that Cas9/PAH can be precisely edited by Cas9/sgRNA in vitro and in vivo to liberate accurately cutted aptamers. We used RCA to prepare PAH containing the sgRNA-binding sequence. The Cas9-mediated degradation of PAH liberated PD-1 DNA aptamers in a prolonged manner at the injection site. PAH/Cas9 exerted a significantly higher antitumor effect compared with free PD-1 aptamer solution or PAH alone. Moreover, the local injection of PAH/Cas9 increased the infiltration of T cells to the tumor site by more than one order of magnitude compared to the other groups.

In the PAH system developed herein, the cleavage of the long RCA-generated template to single units of the PD-1 aptamer was sequence-specifically controlled by sgRNA-guided Cas9 editing of the hydrogel. We previously reported that complementarily bound RCA products can carry and deliver antisense oligonucleotides [23] but improvement was needed in the liberation of antisense oligonucleotides from a single strand after cellular uptake. Another study showed that RCA could protect the encoded aptamers from nuclease-mediated degradation, but this work did not clearly resolve the site-specific release of aptamers [24]. The Cas9/sgRNA-mediated site specific cleavage of RCA products to single-stranded sequences can be widely applied to the delivery of nucleic acids that function as single strands.

Although we herein used the PD-1 aptamer, the concept can be extended to the delivery of antisense oligonucleotides.

We experimentally confirmed that PD-1 aptamers of the correct size were released following Cas9/sgRNA treatment (Fig. IV- 3A, 4B). This specific cleavage of RCA products with Cas9 may help reduce off-target cleavage. In a previous study, CpG sequences were cleaved from RCA products by restriction enzyme treatment [25]: the RCA products were co-administered with restriction enzyme and anti-PD-L1 antibody, which enabled the gradual release of the CpG fragments and the antibody. However, the restriction enzyme-mediated cleavage an aptamer hydrogel can reportedly encounter problems with non-specific cleavage and inconsistencies in the tertiary structure of the released aptamers [26]. Whereas restriction enzymes usually recognize a specific restriction site composed of 4-8 base pairs, Cas9 can recognize 20-base pairs of double-stranded DNA under the guidance of an sgRNA. Thus, Cas9/sgRNA offers an exquisitely specific cutting system [27] that may provide higher precision than that governed by restriction enzymes.

For hydrogel formation, we used two types of RCA templates that differed only in that one contained the sgRNA target sequence while the other harbored the complementary binding sequence. The use of two templates can serve dual purposes. First, the double-stranded sequence generated by base pairing of the RCA products is recognized by Cas9/sgRNA. Second, viscoelasticity is created by the natural crosslinking of RCA loci, forming

the hydrogel. In our previous study, we used an additional condensing molecule (e.g., a cationic peptide) to condense the RCA DNA products by electrostatic interaction [23]. Here, we used endogenous crosslinking between the two RCA strands by hydrogen bonding. Complementary sequence-based DNA hydrogel provided the desirable hydrogel behaviors, such as a higher storage modulus than loss modulus (Fig. IV- 2B), which is a characteristic feature of gel-like materials [28]. Our in vivo study revealed that neither free PD-1 aptamer nor PAH exerted an efficient antitumor effect. For free PD-1 aptamer, this might reflect its rapid degradation and clearance from the injection site and from the body. To prolong the circulation time of the PD-1 aptamer, researchers previously conjugated it to the 5' terminus of 40-kDa polyethyleneglycol [15] The authors found that intraperitoneally administered pegylated PD-1 aptamer suppressed MC-38 (colon carcinoma) cell-derived tumors in an orthotopic tumor model, potentially by extending the half-life of the aptamer. In the present study, we found that intratumorally administered Cas9-edited hydrogel exerted a significantly greater antitumor effect than the free aptamer. The enhanced effect of Cas9/PAH is likely to reflect at least in part the prolonged presence of the PD-1 aptamer as it is gradually liberated from the hydrogel at the tumor site.

Our molecular imaging data support the notion that free PD-1 aptamers injected in solution rapidly disappeared from the injection site. Moreover, it was reported that free aptamers are rapidly cleared from the body due to renal clearance and their instability in biological conditions [16]. PAH

showed a longer retention at the injection site, but did not provide significantly improved antitumor effects compared to those seen in the untreated or PD-1 aptamer solution treated groups. Thus, our data indicate that the Cas9-mediated site-specific liberation of the PD-1 aptamer is needed for the ability to exert efficient anticancer effects.

It would be unlikely that the Cas9/sgRNA used in this study could edit the genome of human cells. Although Cas9/PAH showed a longer retention than free PD-1 aptamer solution in vivo we observed a gradual decrease of imaging density that indicated that Cas9/PAH underwent biodegradation in the body, such as via the actions of endogenous enzymes (e.g., nucleases and proteases). Moreover, the Cas9/sgRNA complex itself is a macromolecule, and thus cannot penetrate into the cytoplasm of cells. Finally, the selected sgRNA sequence reportedly lacks any overlap with the human genome [29].

Finally, we found that the populations of T cells infiltrating the tumor tissues were correlated with the in vivo antitumor effects. Notably, PAH/Cas9 triggered increased infiltration of cytotoxic CD8+ T cells, to a level more than one order of magnitude higher than seen in the other groups. This is likely to reflect the ability of the aptamer to decrease the interaction between PD-1 on immune cells with PD-L1 on tumor cells. B16F10 cells, which were used as a model in the present study, exhibit high-level expression of PD-L1. High-level surface expression of PD-L1 could enable the tumor cells to interact with PD-1-expressing immune cells of the tumor

microenvironment, weakening the activity of these immune cells. Blockade of the interaction between PD-L1 and PD-1 by Cas9-liberated PD-1 aptamers would inhibit this immune cell activity. The results of our in vitro splenocyte study support the notion that the immune checkpoint-blocking interaction between PD-L1 and PD-1 could be inhibited by PD-1 aptamers released from hydrogel by the action of Cas9/sgRNA.

5. References

[1] Sharma P. Allison JP. Immune checkpoint targeting in cancer therapy: toward combination strategies with curative potential. Cell. 2015;161: 205-214.

[2] Topalian SL, Drake CG, Pardoll DM. Immune checkpoint blockade: a common denominator approach to cancer therapy. Cancer Cell. 2015;27:450-461.

[3] Sun C, Mezzadra R, Schumacher TN. Regulation and function of the PD-L1 checkpoint. Immunity. 2018:48:434-452.

[4] Simon S. Labarriere N, PD-1 expression on tumor-specific T cells: Friend or foe for immunotherapy?. Oncoimmunology. 2017;7: e1364828.

[5] Spranger S, Spaapen RM, Zha Y, Williams J, Meng Y, Ha TT, Gajewski TF. Up-regulation of PD-L1, IDO, and T(regs) in the melanoma tumor microenvironment is driven by CD8(+) T cells. Sci. Transl. Med. 2013;5:200ra116.

[6] Hui E, Cheung J, Zhu J, Su X, Taylor MJ, Wallweber HA, Sasmal, DK, Huang J, Kim JM, Mellman I, Vale RD. T cell costimulatory receptor CD28 is a primary target for PD-1-mediated inhibition. Science. 2017; 355:1428-1433.

[7] Tumeh PC, Harview CL, Yearley JH, Shintaku IP, Taylor EJ, Robert, L, Chmielowski B, Spasic M, Henry G, Ciobanu V, West AN, Carmona M,

Kivork C, Seja E, Cherry G, Gutierrez AJ, Grogan TR, Mateus C, Tomasic G, Glaspy JA, Emerson RO, Robins H, Pierce RH, Elashoff DA, Robert C, Ribas A. PD-1 blockade induces responses by inhibiting adaptive immune resistance. Nature. 2014;515:568-571.

[8] Rizvi NA, Hellmann MD, Brahmer JR, Juergens RA, Borghaei H, Gettinger S, Chow LQ, Gerber DE, Laurie SA, Goldman JW, Shepherd FA, Chen AC, Shen Y, Nathan FE, Harbison CT, Antonia S. Nivolumab in combination with platinum-based doublet chemotherapy for first-line treatment of advanced non-small-cell lung cancer. J. Clin. Oncol. 2016; 34:2969-2979.

[9] Gandhi L, Rodriguez-Abreu D, Gadgeel S, Esteban E, Felip E, De Angelis F, Domine M, Clingan P, Hochmair MJ, Powell SF, Cheng SY, Bischoff HG, Peled N, Grossi F, Jennens RR, Reck M, Hui R, Garon EB, Boyer M, Rubio-Viqueira B, Novello S, Kurata T, Gray JE, Vida J, Wei Z, Yang J, Raftopoulos H, Pietanza MC, Garassino MC. Pembrolizumab plus chemotherapy in metastatic non-small-cell lung cancer. N. Engl. J. Med. 2018;378(22):2078-2092.

[10] Koyama S, Akbay EA, Li YY, Herter-Sprie GS, Buczkowski KA, Richards WG, Gandhi L, Redig AJ, Rodig SJ, Asahina H, Jones RE, Kulkarni MM, Kuraguchi M, Palakurthi S, Fecci PE, Johnson BE, Janne PA, Engelman JA, Gangadharan SP, Costa DB, Freeman GJ, Bueno R, Hodi FS, Dranoff G, Wong KK, Hammerman PS. Adaptive resistance to therapeutic PD-1 blockade is associated with upregulation

of alternative immune checkpoints. Nat. Commun. 2016;7:10501.

[11] Arlauckas SP, Garris CS, Kohler RH, Kitaoka M, Cuccarese MF, Yang KS, Miller MA, Carlson JC, Freeman GJ, Anthony RM, Weissleder R, Pittet MJ. In vivo imaging reveals a tumor-associated macrophage-mediated resistance pathway in anti-PD-1 therapy. Sci. Transl. Med., 2017;9(389):eaal3604.

[12] Nelson AL, Dhimolea E, Reichert JM. Development trends for human monoclonal antibody therapeutics. Nat. Rev. Drug Discov. 2010; 9(10): 767-774.

[13] Keefe AD, Pai S, Ellington A. Aptamers as therapeutics. Nat. Rev. Drug Discov. 2010;9(7):537-550.

[14] Nozari A. Berezovski MV. Aptamers for CD antigens: from cell profiling to activity modulation. Mol. Ther. Nucleic Acids. 2017;6: 29-44.

[15] Prodeus A, Abdul-Wahid A, Fischer NW, Huang EH, Cydzik M, Gariepy J. Targeting the PD-1/PD-L1 immune evasion axis with DNA aptamers as a novel therapeutic strategy for the treatment of disseminated cancers. Mol. Ther. Nucleic Acids. 2015; 4:e237.

[16] Lao YH, Phua KK, Leong KW. Aptamer nanomedicine for cancer therapeutics: barriers and potential for translation. ACS Nano. 2015; 9(3):2235-2254.

[17] Prusty DK, Adam V, Zadegan RM, Irsen S, Famulok M. Supramolecularaptamer nano-constructs for receptor-mediated targeting

and light-triggered release of chemotherapeutics into cancer cells. Nat. Commun. 2018;9(1):535.

[18] Wang C, Sun W., Wright G, Wang AZ, and Gu Z. Inflammation-triggered cancer immunotherapy by programmed delivery of CpG and anti-PD1 antibody. Adv. Mater. 2016;28(40):8912-8920.

[19] Shalem O, Sanjana NE, Zhang F. High-throughput functional genomics using CRISPR-Cas9. Nat. Rev. Genet. 2015;16(5):299-311.

[20] Jiang F. Doudna JA. CRISPR-Cas9 structures and mechanisms. Annu. Rev. Biophys. 2017;46:505-529.

[21] Gaj T, Ojala DS, Ekman FK, Byrne LC, Limsirichai P, Schaffer DV. In vivo genome editing improves motor function and extends survival in a mouse model of ALS. Sci. Adv., 2017;3(12): eaar3952. 18

[22] Yin H, Song CQ, Suresh S, Wu Q, Walsh S, Rhym LH, Mintzer E, Bolukbasi MF, Zhu LJ, Kauffman K, Mou H, Oberholzer A, Ding J, Kwan SY, Bogorad RL, Zatsepin T, Koteliansky V, Wolfe SA, Xue W, Langer R, Anderson DG. Structure-guided chemical modification of guide RNA enables potent non-viral in vivo genome editing. Nat. Biotechnol. 2017; 35(12):1179-1187.

[23] Fu Y, Foden JA, Khayter C., Maeder ML, Reyon, D, Joung JK, Sander JD. High-frequency off-target mutagenesis induced by CRISPR-Cas nucleases in human cells. Nat. Biotechnol. 2013;31: 822–826

[24] Noh H, Hu J, Wang X, Xia X, Satelli A, Li S. Immune checkpoint regulator PD-L1 expression on tumor cells by contacting CD11b

positive bone marrow derived stromal cells. Cell Commun. Signal. 2015;13:14.

[25] Juneja, V.R., McGuire, K.A., Manguso, R.T., LaFleur, M.W., Collins, N., Haining, W.N., Freeman, G.J. and Sharpe, A.H. (2017) PD-L1 on tumor cells is sufficient for immune evasion in immunogenic tumors and inhibits CD8 T cell cytotoxicity. J. Exp. Med., 214, 895-904.

[26] Palazón A, Martínez-Forero I, Teijeira A, Morales-Kastresana A, Alfaro C, Sanmamed MF, Perez-Gracia JL, Penuelas I, Hervas-Stubbs S, Rouzaut A, de Landázuri MO, Jure-Kunkel M, Aragones J, Melero I. The HIF-1alpha hypoxia response in tumor-infiltrating T lymphocytes induces functional CD137 (4-1BB) for immunotherapy. Cancer Discov. 2012;2(7):608-623.

[27] Kim MG, Park JY, Shim G, Choi HG, Oh YK. Biomimetic DNA nanoballs for oligonucleotide delivery. Biomaterials, 2015;62:155-163.

[28] Hu R, Zhang X, Zhao Z, Zhu G, Chen T, Fu T, Tan W. DNA nanoflowers for multiplexed cellular imaging and traceable targeted drug delivery. Angew. Chem. Int. Ed. Engl. 2014;53(230:5821-5826.

[29] Wang H. La Russa M, Qi LS. CRISPR/Cas9 in genome editing and beyond. Annu. Rev. Biochem. 2016);85:227-264.

[30] Kamps-Hughes N, Quimby A, Zhu Z, Johnson EA. Massively parallel characterization of restriction endonucleases. Nucleic Acids Res. 2013; 41(11):e119.

[31] Sánchez-Rivera FJ, Jacks T. Applications of the CRISPR-Cas9 system

in cancer biology. Nat. Rev. Cancer. 2015; 5(7):387-395.

[32] Lou J, Liu F, Lindsay CD, Chaudhuri O, Heilshorn SC, Xia Y. Dynamic hyaluronan hydrogels with temporally modulated high injectability and stability using a biocompatible catalyst. Adv. Mater. 2018;30(22): e1705215.

Conclusion

In this study, we developed DAGO, a dsDA-Aptamer and rGObased nano detectors for speedy and specific detection of the target protein in biological and clinical patient samples. Detecting target protein by monitoring changes in fluorescence intensity of a FAM-labeled aptamer that occur upon target binding required minimizing the quenching of FAM fluorescence upon complexation of the aptamer with rGO. This was accomplished by forming a double-stranded structure, and introducing two anchoring moieties. DAGO showed specificity and sensitivity to target protein in serum samples over a five-orders-of-magnitude dynamic range, and was capable of rapidly measuring the concentrations of target protein in patient serum samples with only less than 10 min for whole process. Collectively, our results demonstrate that an rGObased fluorescent aptamer-based DAGO nano detectors could have a wide spectrum of applications for monitoring various target proteins in human clinical samples at a reduced cost and time.

Next, we provided evidence that 7F4D motif can be used for anchoring functional peptide Bu on rGO without hampering its biological property. The use of 4D contributed to minimize the undesirable interaction of Bu with rGO, resulting in the substantially enhanced cell penetrating property of Bu, as compared to native Bu, or 4G spacer residues. These results suggest the wide application of 7F4D motif for non-covalent tethering of functional peptide onto rGO for protein delivery as well as broad spectrum

of peptide-based biosensors on rGO nanosheets.

Lsat we designed an RCA-based DNA hydrogel that can release PD-1 aptamers via Cas9/sgRNA-mediated specific editing. The use of Cas9/sgRNA as a precise editing system means that our system may be broadly applied to various aptamers and single-stranded DNA nucleotides. The hydrogel exhibits prolonged retention at tumorsites in vivo, while its gradual Cas9-mediated liberation of PD-1 aptamers inhibits the activity of immune cells in the tumor microenvironment. Although we used PD-1 aptamers in this study, the Cas9-editedliberation of specific aptamers from RCA products can be used to design systems for the sustained release of other aptamers from RCA DNA hydrogels.

In conclusion, we have utilized GO and RCA based biomaterials for biosensor, anticancer treatment and cancer immunotherapy. Following our study, the utility of functionalized biomaterials indicates the promise to further extend application area of biomedical fileds.

요약

그래핀과 DNA 기반 생체재료의 활용을 통한 진단과 항암 치료 연구

서울대학교 융합과학기술대학원
분자의학 및 바이오제약학과
분자의학 및 바이오제약학 전공
이재우

질병의 진단과 치료에 있어서 생체재료의 활용은 최근 그 분야를 넓혀 가고 있으며, 특히 생체적합성의 특징으로 인해 부작용을 최소화 하는 물질로 각광받고 있다. 그래핀 옥사이드 나노 시트는 그 자체의 표면적이 넓고 풍부한 자유전자로 인해 아로마틱 링 구조를 가진 화합물질과 결합력이 뛰어나다. 뿐만 아니라 DNA 단일가닥, 지질사슬과도 뛰어난 결합력을 가지므로 다양한 물질로 표면 수식이 가능하다. 이러한 물질들로 표면이 수식되면 생체내 안정성을 증진 될 뿐만 아니라 세포내 침투력을 강화시켜 약물전달을 효율적으로 시킬 수 있다. 그래핀 표면의 수식 방법 및 수식 물질에 의해 변화무쌍하게 활용될 수 있으며 그 효율

또한 극대화 시킬 수 있다. 본 논문에서는 아로마틱 링 구조를 포함한 페닐알라닌 펩타이드를 활용하여 그래핀 나노 시트의 약물 전달체로서의 효과를 극대화시켰으며, 그 수식 방법을 간소화 함으로써 활용범위를 다변화 시켰다. 7개의 페닐알라닌 잔기를 기능성 펩타이드(세포 침투 보조 펩타이드)에 추가하여 키메릭 펩타이드를 합성하였고, 이를 그래핀 나노 시트에 파이-파이 결합으로 수식하여 세포내 침투율을 높혔다. 근적외선을 쪼여 줌으로써 그래핀의 광열효과까지 확인하였다.

그래핀 옥사이드 나노시트에 특정 물질 감응형 aptamer를 형광과 함께 수식하면 질병의 진단영역에 활용할 수 있다. 그래핀 옥사이드는 형광물질과 쉽게 결합하며 발광을 억제 시킬 수 있는 생체재료이다. 형광물질에 DNA 이중가닥을 수식시키면 그래핀으로부터 이격되어 발광을 유지시킬수 있는 원리를 이용하여 DNA-그래핀 기반 질병 진단체를 개발하였다. DNA 이중가닥은 특정 물질에 감응하여 단일가닥으로 해체되고 그로 인해 단일가닥 DNA에 수식되어 있는 형광은 물질 특이적으로 빛을 잃게 된다. 본 연구에서는 인터페론 감마 특이적 aptamer를 활용하여 HIV 진단체를 설계하였다.

마지막으로 Rolling circle amplification(RCA) 법을 활용한 DNA중합체는 생체적합한 물질일 뿐만 아니라 생분해성이기에 약문전달분야에서 널리 활용되고 있다. 무엇보다 그 서열의 조작이 용이하여 다양한 결과물을 생산할 수 있어 그 용도가 무궁무진하다. 본 연구에서는 RCA-DNA 중합체를 면역항암치료에 접목하였다. 뿐만 아니라 정교한 유전자 가위인 CRISPR Cas9을 도입하여 RCA-DAN 중합체가 생체 내에서 정

확한 서열의 치료 aptamer(PD-1 aptamer)를 방출하도록 하였다. 그 결과 대조군 대비 뛰어난 항암 면역치료 효과를 확인할 수 있었으며, 이 시스템을 활용하여 다양한 aptamer의 항암 치료 효과 극대화를 기대해 본다.

주요어: Graphene oxide, Diagnosis, Chimeric peptide, Photothermal therapy, Cas9 editing, PD1 DNA polyaptamer hydrogel, Immune checkpoint blockade, Immunotherapy

학 번: 2011-23064